Multidecadal wind-driven shifts in northwest Pacific temperature, salinity, O2 , and PO4

Eun Young Kwon, Young Ho Kim, Young-Gyu Park, Young-Hyang Park, John Dunne, Kyung-Il Chang

AGU PUBLICATIONS

Global Biogeochemical Cycles

RESEARCH ARTICLE
10.1002/2016GB005442

Key Points:
- Historical data indicate southward shifts in O_2 and PO_4 from 1968 to 2007
- The gyre shift can explain O_2 and PO_4 variability within gyre boundaries
- High-resolution climate model supports the observation-based finding

Supporting Information:
- Supporting Information S1

Correspondence to:
E. Y. Kwon,
eykwon76@gmail.com

Citation:
Kwon, E. Y., Y. H. Kim, Y.-G. Park, Y.-H. Park, J. Dunne, and K.-I. Chang (2016), Multidecadal wind-driven shifts in northwest Pacific temperature, salinity, O_2, and PO_4, *Global Biogeochem. Cycles*, *30*, 1599–1619, doi:10.1002/2016GB005442.

Received 5 MAY 2016
Accepted 12 OCT 2016
Accepted article online 15 OCT 2016
Published online 3 NOV 2016

Multidecadal wind-driven shifts in northwest Pacific temperature, salinity, O_2, and PO_4

Eun Young Kwon[1], Young Ho Kim[2], Young-Gyu Park[2], Young-Hyang Park[3], John Dunne[4], and Kyung-Il Chang[1]

[1]Research Institute of Oceanography, Seoul National University, Seoul, South Korea, [2]Physical Oceanography Division, Korea Institute of Ocean Science & Technology, Ansan, South Korea, [3]LOCEAN, UMR 7159, CNRS/UPMC/MNHN/IRD, Université Pierre Marie Curie, Paris, France, [4]Geophysical Fluid Dynamics Laboratory, National Oceanic and Atmospheric Administration, Princeton, New Jersey, USA

Abstract The North Pacific gyre boundaries are characterized by stark contrasts in physical and biogeochemical properties. Meridional movement of gyre boundaries, influenced by climate change, can therefore exert a large influence not only on marine ecosystems but also on climate. We examine the evidence for wind-driven southward shifts in subsurface temperature, salinity, PO_4, and O_2 within the northwest Pacific from the 1950s to the 2000s. Gyre boundary shifts can explain 30–60% of temperature and salinity trends zonally averaged in the northwest Pacific and observed PO_4 and O_2 trends along the 137°E and 144°E meridians. The close tie between the wind-driven shifts in gyre boundaries and the tracer distributions is further supported by results from an eddy-resolving (0.1° × 0.1°) Geophysical Fluid Dynamics Laboratory climate model, suggesting that the physical and biogeochemical properties averaged within the northwest Pacific gyre boundaries closely follow the latitude changes of the zero Sverdrup stream function with lags of 0 to 3 years. The gyre shift effect on tracer distribution is poorly represented in a coarse resolution (1° × 1°) model due partly to poor representations of fronts and eddies. This study suggests that future changes in northwest Pacific PO_4 and O_2 content may depend not only on ocean temperature and stratification but also on the ocean gyre response to winds.

1. Introduction

Upper ocean distributions of physical and biogeochemical properties are partly shaped by wind-driven gyre systems. Because no major deep and bottom waters form in the high-latitude North Pacific, the North Pacific subpolar thermocline has low O_2 and high PO_4 that result from Ekman upwelling (Figure 1). On the other hand, O_2-rich and PO_4-depleted surface waters subduct into the subtropical thermocline [*Palter et al.*, 2005; *Kwon et al.*, 2016]. Due to these contrasting features, physical and biogeochemical characteristics change dramatically across gyre boundaries. The northern boundary of the North Pacific subtropical gyre is located around 45°N corresponding to the maximum strength of the westerlies, while the southern boundary is around 15°N corresponding to the maximum strength of the trade winds. The strength and position of the midlatitude and low-latitude winds have varied over multidecadal timescales, with far-reaching impacts on the physical properties of seawater within gyre boundaries, and North Pacific marine ecosystems and climate [e.g., *Mantua et al.*, 1997; *Deser et al.*, 1999; *Joyce and Dunworth-Baker*, 2003; *Kwon et al.*, 2010; *Chen and Wu*, 2012; *Nakanowatari et al.*, 2015].

Northwest Pacific circulation and physical properties have varied on multidecadal timescales in concert with wind changes. By comparing subsurface temperature and salinity averaged over the two time periods (1945–1975 and 1976–1998), *Joyce and Dunworth-Baker* [2003] found cooling and freshening trends of up to 2°C and 0.2 psu within the transition area between the subtropical and subpolar gyres. They suggested that the multidecadal trends in the physical properties are consistent with a southward shift of the Kuroshio Bifurcation Front and that the variation in the frontal position is correlated with the North Pacific wind change. *Nonaka et al.* [2006] and *Taguchi et al.* [2007] also reported overall southward shifts in the Kuroshio Extension and the subtropical recirculation gyre from 1950 to 2003 using a high-resolution ocean model forced by historical wind stress data. In association with wind stress curl changes in low latitudes, *Chen and Wu* [2012] reported an overall southward shift of the bifurcation latitude of the Pacific North Equatorial Current, which marks the southern boundary of the subtropical gyre, from 1950 to 2008. Despite the evidence for the wind-driven changes in circulation and physical properties in the northwest

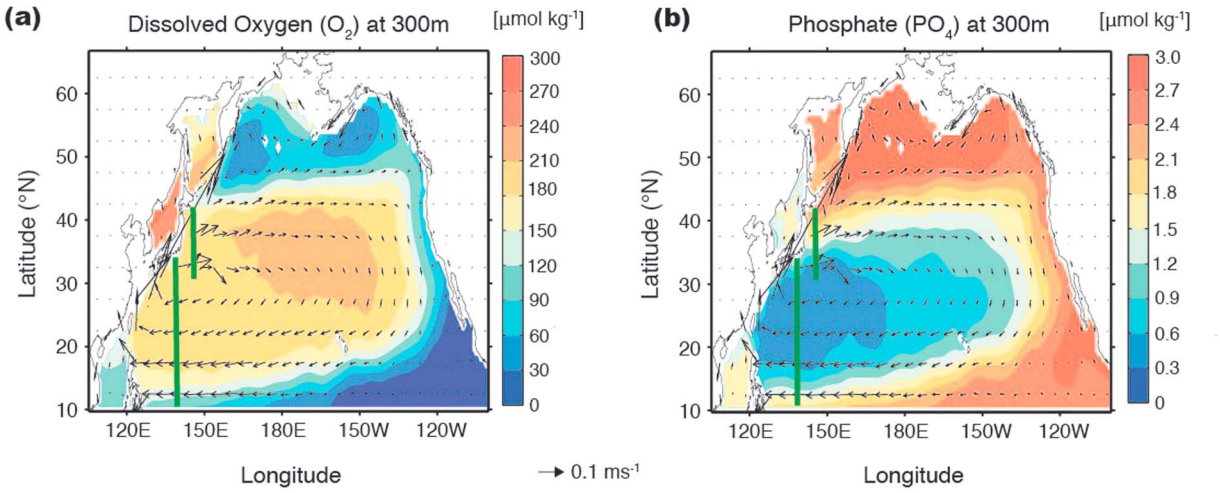

Figure 1. Annual mean distributions at a depth of 300 m for (a) dissolved O_2 and (b) PO_4. Data are obtained from the 1°×1° gridded World Ocean Atlas 2013. Vectors represent the water flow, interpolated to a depth of 300 m from the Simple Ocean Data Assimilation (SODA) simulation. Green solid lines indicate the sections at which the vertical structures are shown in Figure 3.

Pacific, the southward shift of the Kuroshio Bifurcation Front has been regarded as being discordant with observed O_2 changes [*Joyce and Dunworth-Baker*, 2003] or suggested to be important only on local scales [*Emerson et al*., 2004; *Deutsch et al*., 2005]. As for the southern boundary, the effect of the meridional shift on biogeochemical properties remains poorly understood.

In the northwest Pacific, large changes in biogeochemical properties have occurred over the past decades. Between 1968 and 1998, apparent oxygen utilization (AOU) has increased (O_2 has declined) by 0.9 ± 0.5 μmol $O_2\,kg^{-1}\,yr^{-1}$, while PO_4 has increased by 0.005 ± 0.003 μmol $PO_4\,kg^{-1}\,yr^{-1}$ in the subsurface water of the transition area (40°–42°N) off the east coast of Japan [*Ono et al*., 2001; *Watanabe et al*., 2003]. The O_2 and PO_4 variability within the transition area has been shown to correlate well with the multidecadal variations in midlatitude winds as represented by the North Pacific Index [*Watanabe et al*., 2003]. Similarly decreasing O_2 and increasing PO_4 were also reported within the eastern subpolar gyre between the 1950s and the 2000s [*Whitney et al*., 2007, 2013]. While decreasing O_2 in the subpolar gyre has been attributed to reduced ventilation rates from the sea surface [*Emerson et al*., 2004; *Deutsch et al*., 2005; *Andreev and Baturina*, 2006; *Nakanowatari et al*., 2007], a study using a box model suggested that increasing PO_4 in the subpolar gyre is the biological response to warming and O_2 loss within the thermocline [*Whitney et al*., 2013]. On the other hand, *Tadokoro et al*. [2009] attributed the variations in PO_4 within the transition area to increasing upper ocean stratification superimposed on decadal variations in intermediate water formation rates.

Unlike the ubiquitous declining trends in O_2 within the subpolar gyre, O_2 trends in the subtropical gyre are less pronounced and depend on latitudes, water masses, and the time frames considered [e.g., *Takatani et al*., 2012; *Sasano et al*., 2015; *Kwon et al*., 2016]. For example, *Emerson et al*. [2004] and *Deutsch et al*. [2005] suggested that AOU within the subtropical thermocline south of ~30°N was lower (O_2 was higher) in the 1990s than in the 1980s due to southward expansion of the subtropical gyre. *Stramma et al*. [2012] also showed that O_2 has increased by ~0.2 μmol $O_2\,kg^{-1}\,yr^{-1}$ at 300 m of the subtropical gyre between 1960 and 2010. On the other hand, *Takatani et al*. [2012] and *Sasano et al*. [2015] suggested that O_2 has overall decreased by 0.2–0.4 μmol $O_2\,kg^{-1}\,yr^{-1}$ in the northwest Pacific at the 137°E and 165°E meridians since the late 1980s. While the decreasing trends were most pronounced within the northern subtropical gyre, which was attributed to warming and the advection of O_2-depleted water, increasing O_2 was also reported south of the subtropical gyre 5°–10°N over the same time period [*Sasano et al*., 2015]. A more comprehensive analysis based on a compiled historical data set was conducted by *Helm et al*. [2011] who showed that dissolved O_2 averaged throughout the upper ocean (100–1000 m) has slightly increased within the subtropical gyre of the northwest Pacific from 1970 to 1992.

Compared to studies of dissolved O_2, less attention has been paid to understanding multidecadal PO_4 changes in the northwest Pacific subtropical gyre, probably due to technical challenges in detecting small

PO_4 changes from the PO_4-depleted subtropical thermocline water. Nevertheless, a study using time series data reported that PO_4 has decreased in the central subtropical gyre off Hawaii between 1968 and 1997 [*Karl et al*., 2001]. However, the spatial extent of subtropical PO_4 change and the cause have not yet been explored. Given that PO_4 is a crucial nutrient for the primary production that forms the base of the food webs, understanding PO_4 variability and its relation to climate can help understand marine ecosystems in changing climates. Subsurface PO_4 is composed of two components: preformed PO_4 that is transported from the sea surface by ocean circulation and remineralized PO_4 that is added to the water column by decomposition of organic matter. Because remineralized PO_4 beneath the euphotic zone is closely tied to the biological consumption of O_2, PO_4 variability can be linked to O_2 variability via respiration [*Redfield*, 1934; *Anderson and Sarmiento*, 1994]. Changes in ocean circulation can also make coordinated changes in PO_4 and O_2 due to water mass redistribution especially within gyre boundaries. Therefore, coanalyses of physical and biogeochemical properties can help elucidate the mechanisms for the PO_4 and O_2 variability.

In this study, we use historical data sets to diagnose past changes in northwest Pacific O_2 and PO_4 between 10°N and 45°N from 1968 to 2007. Nearly continuous records have been made available since 1967 with reasonably good coverage of the northwest Pacific. This continuity allows us to explore multidecadal variations in O_2 and PO_4 with statistically significant trend estimates between 1968 and 2007. Our analysis of O_2 and PO_4 is supplemented by the use of observationally constrained simulations of temperature, salinity, and winds. Unlike most of previous studies carried out on constant density layers [e.g., *Ono et al*., 2001; *Emerson et al*., 2004; *Deutsch et al*., 2005; *Nakanowatari et al*., 2007; *Kwon et al*., 2016], our analysis is based on constant depth layers in order to focus on potential effects of ocean circulation change on tracer distributions. While analyses along constant density surfaces are more suitable for detecting the effects of ocean ventilation changes, any frontal changes tend to be smoothed out due to strong advection and eddy mixing along constant density surfaces. On the other hand, biogeochemical properties along constant depth surfaces show stark contrasts across frontal regions (Figure 1), which may prove to be a more suitable framework in which we can study the effects of water mass redistributions and possible gyre shifts.

As will be shown below, this study reveals synchronous trends in temperature, salinity, O_2, and PO_4 within the northwest Pacific between 10°N and 45°N, which is consistent with a southward shift of the subtropical gyre driven by wind changes. Building on the previous work highlighting the effect of wind-driven gyre shifts on physical properties [*Seager et al*., 2001; *Joyce and Dunworth-Baker*, 2003; *Chen and Wu*, 2012], we suggest that the meridional shifts in subtropical gyre boundaries may provide a unifying framework to understand multidecadal variations in temperature, salinity, O_2, and PO_4 in the northwest Pacific over the past decades, not only within the midlatitude transition area but also within the southern subtropical thermocline.

While our analysis of historical data sets helps us understand the northwest Pacific O_2 and PO_4 variability over the past half century, an uncertainty arises in the observation-based study due to sparse temporal and spatial coverage of observations. In order to overcome this limitation, we also use the state-of-the-art climate model CM2.6 [*Griffies et al*., 2015] coupled with a simple representation of O_2 and PO_4 cycles [*Galbraith et al*., 2015], developed by the NOAA's Geophysical Fluid Dynamics Laboratory (GFDL). Using a control simulation of the CM2.6 model, which is run with preindustrial radiative conditions, we demonstrate that temperature, salinity, PO_4, and O_2 averaged within the northwest Pacific gyre boundaries are highly correlated with the meridional movement of gyre boundaries with lags of 2 to 3 years. The model's ability to represent the wind-driven gyre shift effects on the physical and biogeochemical tracers is also tested using a coarse resolution climate model, ESM2M [*Dunne et al*., 2012, 2013].

The rest of this paper is organized as follows: In section 2, we describe methods and models employed in this study. Historical multidecadal trends in PO_4 and O_2 are described in section 3, followed by a description of historical changes in temperature and salinity in section 4. In section 5, we show results from the CM2.6 model. Section 6 discusses and summarizes this study.

2. Methods

2.1. Trends for Observed O_2 and PO_4

We use quality-controlled bottle data sets for O_2 and PO_4 from the World Ocean Database 2013 [*Boyer et al*., 2013]. Discrete O_2 and PO_4 data are interpolated into standard depths using a depth interval of 50 m below

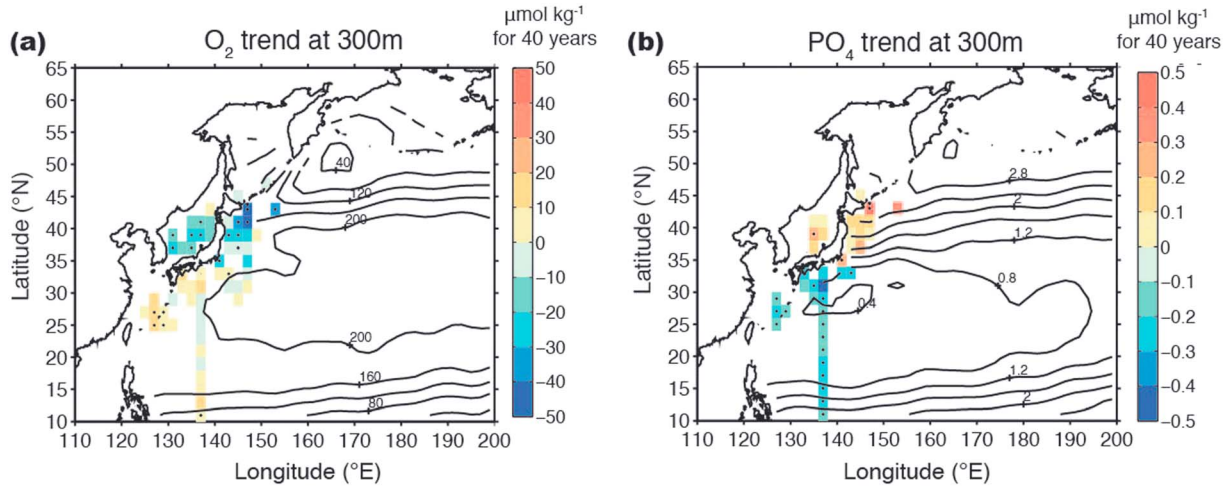

Figure 2. Linear trends for O_2 and PO_4 at 300 m from 1968 to 2007, computed using the World Ocean Database 2013 with a grid size of 2° × 2°. (a) Linear trends for O_2. Color shading represents trends over the past 40 years at grid points where observations are available for the entire 10 temporal bins. (b) The same as Figure 2a except that linear trends for PO_4 are shown. Grid points with values significant at the 90% confidence level are marked with black dots. Black solid lines are climatological mean fields from the World Ocean Atlas 2013.

the winter mixed layer depth of 150 m. The interpolated values are then gridded with grid sizes of 2° latitude × 2° longitude (to produce maps in Figure 2) and 1° latitude (to produce vertical sections in Figure 3). Additional quality control is performed at each grid point by removing data outliers that exceed ±3 standard deviations calculated within ±2.5° latitude and ±2.5° longitude, an approach similar to that of *Takatani et al.* [2012]. All quality-controlled data within each grid point are averaged using a temporal resolution of 4 years, beginning with 1968. Therefore, between 1968 and 2007, maximum 10 temporal bins represent time evolutions of O_2 and PO_4 for each grid point. To obtain linear trends between 1968 and 2007, we perform a simple linear regression analysis for the grid points where no empty temporal bin exists. Two meridional sections with the largest data pools are chosen to represent the vertical sections for the northwest Pacific, including a section at 137 ± 0.1°E between 10°N and 35°N and a section at 144 ± 0.1°E between 30°N and 43°N (Figure 1). Due to the small number of samples (10 samples per each grid), we perform a Student's *t* test using a moderate significance level of 90% in order to determine uncertainty ranges for the linear trends.

2.2. Analyses of Simple Ocean Data Assimilation and World Ocean Atlas 2013

To explore multidecadal variations in temperature and salinity, we use an observationally constrained simulation, the Simple Ocean Data Assimilation (SODA) version 2.2.4 [*Carton et al.*, 2000a, 2000b; *Carton and Giese*, 2008]. The SODA2.2.4 is based on Parallel Ocean Program numerics [*Smith et al.*, 1992], forced by 20CRv2 surface wind stress [*Compo et al.*, 2011], and heat and freshwater fluxes determined by bulk formulas. The SODA2.2.4 has a horizontal resolution of 0.25° × 0.4° and 40 vertical levels. The vertical resolution ranges from 10 m near the surface to ~250 m near the bottom. The model solutions of temperature, salinity, and flow fields are remapped onto uniform 0.5° × 0.5° horizontal grid points [*Carton and Giese*, 2008]. An optimal interpolation method has been applied to assimilate in situ temperature and salinity profiles and satellite-borne sea surface temperature [*Carton and Giese*, 2008]. This feature allows the model to reasonably capture observed large-scale upper ocean physical structures and circulations [*Carton et al.*, 2000b; *Chen and Wu*, 2012].

To explore the consistency among different reanalysis products, we also use SODA2.1.6 and EN4 data sets to diagnose past changes in northwest Pacific temperature and salinity. SODA2.1.6 is similar to the SODA2.2.4 except that the model is forced by ERA-40 and ERA-interim surface winds [*Carton and Giese*, 2008]. EN4 provides objectively analyzed monthly mean fields of temperature and salinity with a horizontal resolution of 1° × 1° and a vertical resolution ranging from 10 m near the surface to 300 m near the bottom [*Good et al.*, 2013]. EN4 uses an optimal interpolation method based on quality-controlled profile data. Temperature and salinity fields over time periods of 1950–2008, 1958–2007, and 1947–2013 are analyzed for SODA2.2.4,

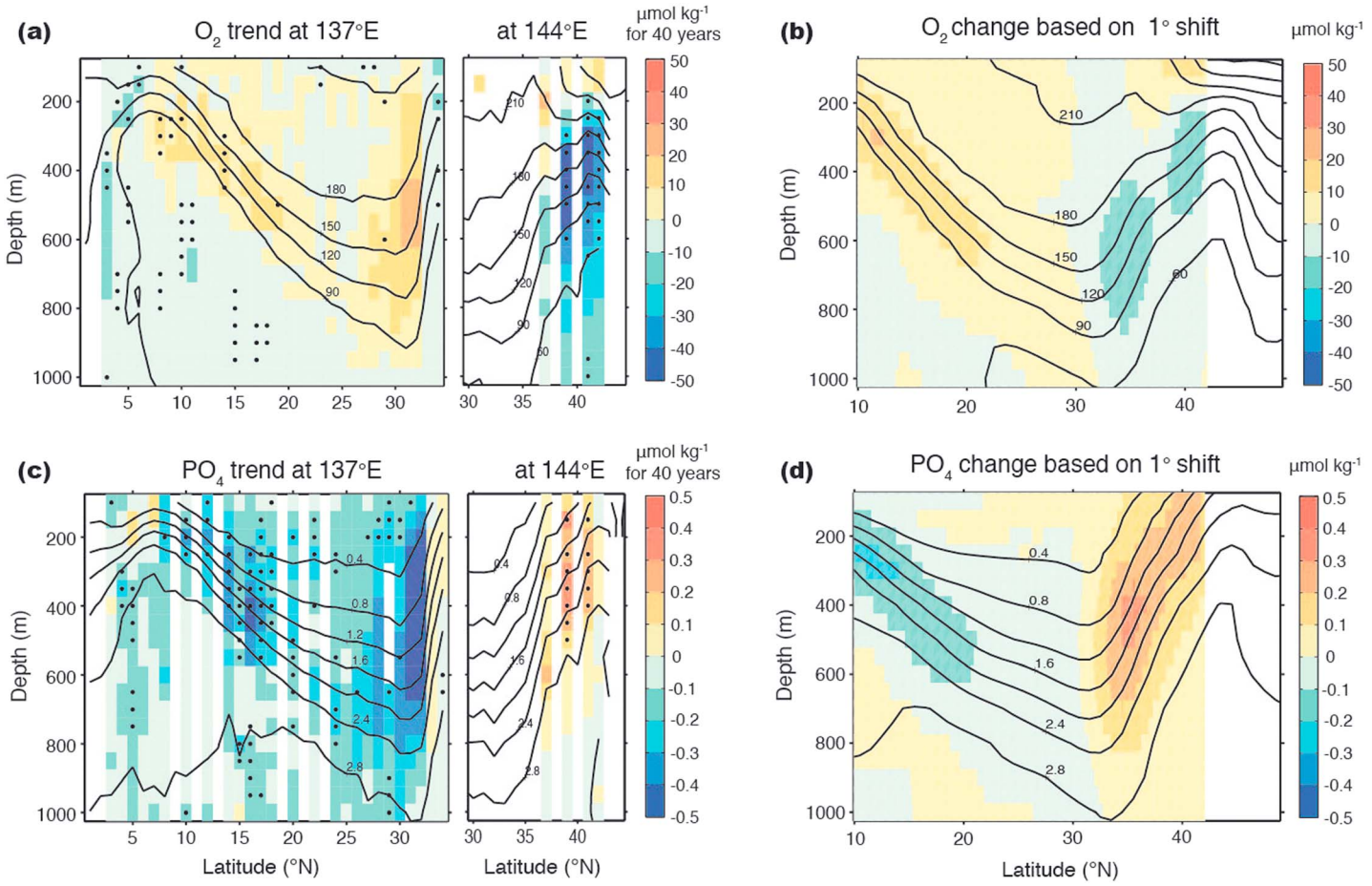

Figure 3. Vertical sections for the O_2 and PO_4 trends from 1968 to 2007. (a) Linear trends of O_2 at the sections shown in Figure 1 (3°–34°N at 137±0.1°E and 30°–42°N at 144±0.1°E), computed using the World Ocean Database 2013. Linear trends (color shading) are computed only for the grid points where observations are available for the entire 10 temporal bins. Trends significant above the 90% confidence level are marked with black dots. Contour lines represent the climatological mean distribution of O_2, computed using the same data set. (b) The O_2 change that would have been obtained if the climatological mean distribution for O_2 at 150°E has shifted to the south by 1°, computed using the World Ocean Atlas 2013; i.e., the climatological mean is subtracted from the hypothetical case, for which the same climatological distribution between 10°N and 43°N has been shifted to the south by 1°. The climatological mean is shown with black solid lines, while the O_2 difference is shown with color shading. (c) The same as Figure 3a except that linear trends for PO_4 are shown. (d) The same as Figure 3b except that a southward shift for PO_4 is shown.

SODA2.1.6, and EN4, respectively. Linear trends for the SODA-based estimates are determined by performing a simple linear regression analysis of annual mean values over the entire time periods. A Student's *t* test is performed in order to determine uncertainty ranges for linear trends using a 95% significance level.

Multidecadal changes in temperature and salinity can also be assessed using the objectively analyzed climatological data, the World Ocean Atlas 2013 (WOA) [*Locarnini et al*., 2013; *Zweng et al*., 2013]. We use the 1° × 1° decadal mean (1955–1964, 1965–1974, 1975–1984, 1985–1994, 1995–2004, and 2005–2012) temperature and salinity fields available at https://www.nodc.noaa.gov/OC5/woa13/woa13data.html to compute multidecadal differences of the decadal mean fields. The WOA climatological mean (1955–2012) fields of O_2 and PO_4 are also used to examine the climatological mean distributions in Figures 1a and 1b and to evaluate the gyre shift effects in Figures 3b and 3d.

2.3. The CM2.6 Model

CM2.6 is a coupled climate model first introduced by *Delworth et al*. [2012] and further analyzed by *Griffies et al*. [2015]. The model uses an atmospheric component of roughly 50 km horizontal resolution, as well as sea ice and land model components. The oceanic component is based on the Modular Ocean Model version 5 (MOM5 [*Griffies*, 2012]) run with volume-conserving Boussinesq kinematics and a *z** vertical coordinate. The

vertical resolution is 50 levels with a thickness of 10 m at the surface increasing with depth to 210 m. The horizontal grid spacing is 0.1° × 0.1°, corresponding to a grid size of 5.5 km at 60°N. The submesoscale mixed layer eddy parameterization of *Fox-Kemper et al*. [2011] is applied to account for the restratification effect of submesoscale eddies in the mixed layer that the 0.1° horizontal grid spacing is not able to resolve. However, so as not to dilute the explicit role of mesoscale eddies, no mesoscale eddy transport parameterization for thickness mixing is applied. This allows us to focus directly on large and mesoscale processes that are explicitly resolved in the model. A simplified version of the prognostic biogeochemical model BLING [*Galbraith et al*., 2010], called miniBLING, is coupled to CM2.6, which includes three prognostic tracers, namely, dissolved inorganic carbon, a dissolved inorganic macronutrient (called PO_4), and dissolved oxygen (O_2). See *Galbraith et al*. [2015] for a description of the biogeochemical component (miniBLING) and *Dufour et al*. [2015] for description and assessment of the overall physical and biogeochemical simulation characteristics.

2.4. Computing the Sverdrup Stream Function

According to Sverdrup theory [*Sverdrup*, 1947], the stream function, depicting a depth-integrated wind-driven gyre circulation, can be written as $\psi(x) = -\frac{f}{\beta\rho_0}\int_{x_E}^{x} k\cdot\left(\nabla\times\frac{\tau}{f}\right)dx'$ where f is the Coriolis parameter, β is the meridional gradient of f, ρ_0 is the mean surface density, k is the unit vector in the vertical direction, τ is the wind stress vector, and x_E is the eastern boundary of the ocean basin. Geostrophic transport occurs along the contour lines of the stream function in the clockwise direction when the stream function is positive and in the counterclockwise direction when the stream function is negative. The Sverdrup stream function is computed based on annual mean wind stress from the 20CRv2 [*Compo et al*., 2011] and the CM2.6 model. In order to reduce computational cost when calculating the annual mean Sverdrup stream function and its empirical orthogonal function (EOF) from the CM2.6 wind stress, we average the 0.1° × 0.1° annual mean wind stress onto 1° × 1° grid points. The latitude of the zero Sverdrup stream function is then determined by linearly interpolating the zonally averaged (140°–180°E) Sverdrup stream function. Throughout this study, a low-pass filter based on the Lanczos filtering method with a cutoff frequency of 10 years [*Duchon*, 1979] is used to obtain a low-frequency component of temporal variations.

3. Historical O_2 and PO_4 Trends

Figure 2 shows horizontal maps for the O_2 and PO_4 trends at 300 m computed using the observations. Nearly continuous measurements have been made west of 150°E (Figure 2), providing most reliable estimates for the linear trends between 1968 and 2007. Consistent with *Ono et al*. [2001], O_2 has decreased and PO_4 has increased off the east coast of Hokkaido. Similar decreasing O_2 and increasing PO_4 have occurred in the East/Japan Sea, despite the fact that the exchange of water between the marginal sea and the open ocean is limited to depths shallower than ~250 m by narrow straits [*Watanabe et al*., 2003]. On the other hand, O_2 has remained nearly constant or slightly increased south of Japan at 300 m. An increasing O_2 trend becomes significant near the southern boundary of the subtropical gyre, 10°–15°N, which is in accord with *Sasano et al*. [2015]. Over the same time period, significantly decreasing trends in PO_4 are found between 10°N and 34°N. Combined with increasing PO_4 within the transition area, decreasing PO_4 in the subtropics forms a dipole structure of the northwest Pacific PO_4 trend. A similar dipole structure of the O_2 trend is also evident between the transition area and the southern subtropical gyre, although most of the O_2 trends in the subtropical gyre are not significant at the 90% confidence level.

The O_2 and PO_4 trends at the two vertical sections (10°–34°N at 137 ± 0.1°E and 30°–42°N at 144 ± 0.1°E; see Figure 1) are also characterized by dipole structures with opposite signs between the subtropical gyre at 137 ± 0.1°E and the midlatitude transition area at 144 ± 0.1°E (Figures 3a and 3c). In general, dissolved O_2 has decreased within the transition area and increased within the subtropical gyre between 1968 and 2007. At the same time, PO_4 has increased near 40°N and has decreased south of 34°N. If we consider the linear trends significant at a 90% confidence level only, O_2 has decreased by an average of 0.83 ± 0.27 μmol O_2 kg^{-1} yr^{-1} while PO_4 has increased by 0.0054 ± 0.0039 μmol PO_4 kg^{-1} yr^{-1} within the transition area, which agrees with *Ono et al*. [2001]. Within the subtropical gyre, the averaged PO_4 trend is estimated to be −0.0050 ± 0.0019 μmol PO_4 kg^{-1} yr^{-1}, with the most pronounced decreasing trends occurring along the subsurface PO_4 front where the meridional and vertical gradients for the climatological mean PO_4 distributions are large.

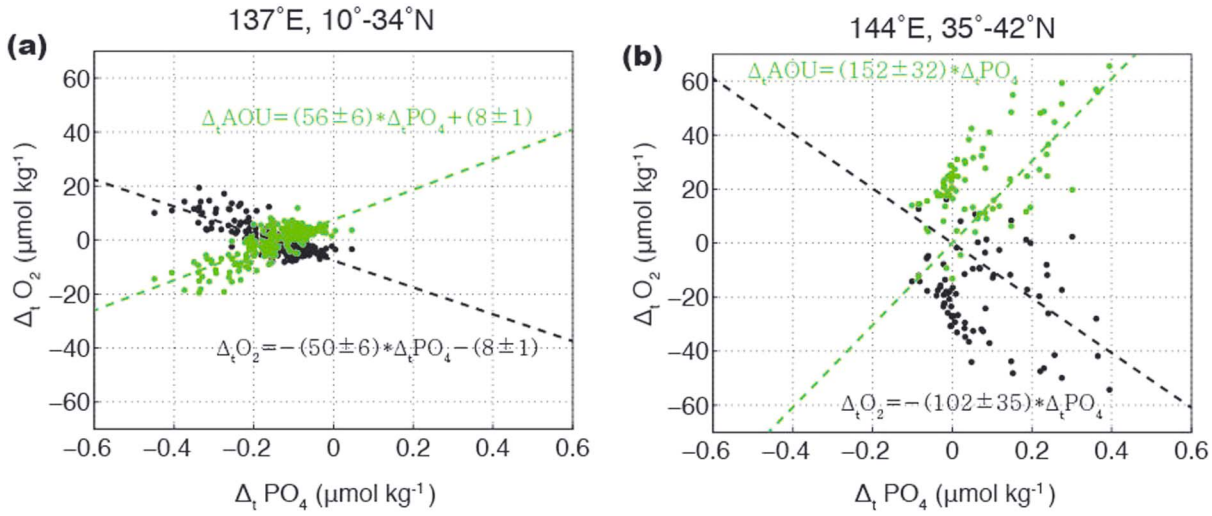

Figure 4. Scatterplots of the linear trend for O_2 ($\Delta_t O_2$) versus the linear trend for PO_4 ($\Delta_t PO_4$). (a) Black dots show the linear trend for O_2 ($\Delta_t O_2$) versus the linear trend for PO_4 ($\Delta_t PO_4$), taken from the 137±0.1°E section in Figures 3a and 3c (subtropics). Black dashed line indicates a linear fit to black dots. Green dots show the linear trend for AOU (Δ_tAOU) versus the linear trend for PO_4 ($\Delta_t PO_4$) taken from the same section. Green dashed line indicates a linear fit to green dots. The ± values represent uncertainties at the 95% significance level. (b) The same as Figure 4a except that the ratio of the linear trends taken from the 144±0.1°E section in Figures 3a and 3c (transition area) is shown.

Similarly, the most pronounced increasing trends of O_2 occur within the subsurface O_2 front where the meridional and vertical gradients for the climatological mean O_2 distributions are large. The averaged trend for the subtropical O_2 is 0.29 ± 0.12 μmol O_2 kg^{-1} yr^{-1} when only positive trends significant at 90% are averaged. The dipole pattern of the northwest Pacific O_2 trend (Figure 3a) qualitatively agrees with the O_2 trends averaged in the upper water (100–1000 m) of the northwest Pacific mapped by *Helm et al*. [2011] [see *Helm et al*., 2011, Figure 1].

Taken together, regions with increasing O_2 concentrations roughly coincide with regions containing decreasing PO_4 concentrations, and vice versa. A potential cause for these opposing trends in O_2 and PO_4 could be changes in subsurface biological respiration, resulting from local changes in productivity, accumulated respiration rates, or the transit time of water from the surface. If such a change is a primary cause, and the stoichiometry of remineralization and watermass contributions are effectively constant, the ratio for the linear trends will follow a stoichiometric ratio for remineralization, the ratio at which O_2 is consumed with respect to a unit increase in remineralized PO_4. We find that the ratio of O_2 trend to PO_4 trend falls roughly below the reported stoichiometric ratios for remineralization. The ratio of the two trends ($-\Delta_t O_2/\Delta_t PO_4$) has a range of 44–56 in the subtropics (Figure 4a), far below a global average, $-rO_2{:}P = 170 \pm 10$ [*Anderson and Sarmiento*, 1994]. This is the case even when the spatial variations of $-rO_2{:}P = 100$–200 are considered [*DeVries and Deutsch*, 2014]. On the other hand, the ratio of the two trends ($-\Delta_t O_2/\Delta_t PO_4$) has a range of 67–137 within the transition area (Figure 4b), which is slightly higher and more scattered than that we diagnose in the subtropics but still falls below or within the lower bound of most reported stoichiometric ratios for large ocean areas (see section 6 for a further discussion of O_2 trend within the transition area). The use of AOU instead of O_2 does not make any significant difference in terms of the ratio of the two temporal trends (Figures 4a and 4b).

The linear trends shown in Figure 3 hide some interesting features of O_2 and PO_4 variability occurring on interannual to decadal timescales. Figure 5 shows the O_2 and PO_4 time series, averaged over 200–600 m at each latitudinal grid point of the 137 ± 0.1°E and 144 ± 0.1°E meridians. We find that the interannual to decadal variability differs with latitudes and in some cases with depths (see also supporting information Figures S1–S4 for the O_2 and PO_4 time series that the trend estimates in Figures 3a and 3c are based on). This highly variable nature of interannual variations, which depends on sampling locations, may partly indicate the influence of small-scale processes on tracer distributions in the western boundary current system. Despite the heterogeneity, we find that the temporal anomalies of O_2 and PO_4 are strongly correlated with one another. The correlation coefficients between PO_4 anomalies (with respect to their time mean values) and O_2

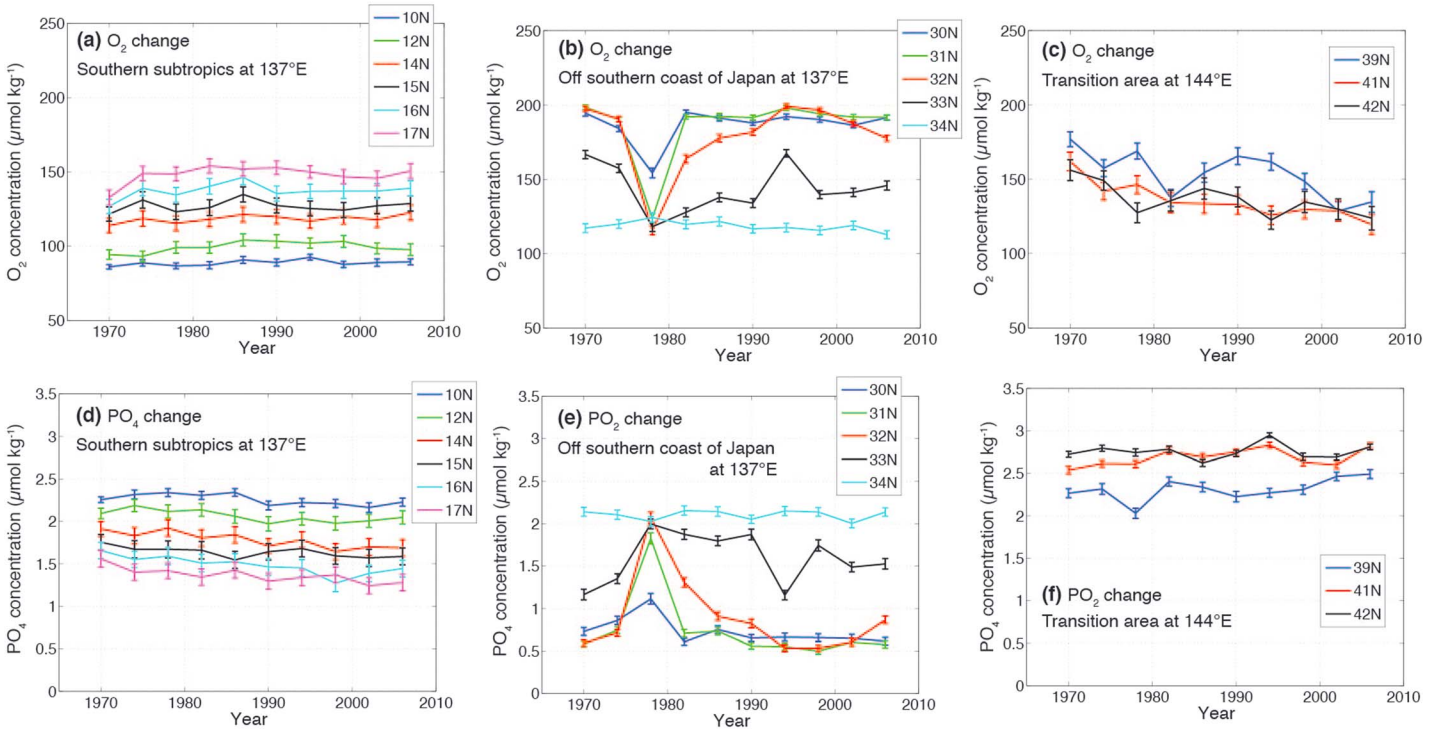

Figure 5. Time series of O_2 and PO_4 at the 137±0.1°E and 144±0.1°E meridians. Gridded O_2 data are averaged over 200–600 m at each 1° latitudinal grid point using a 4 year time resolution. For example, an O_2 concentration at $t = 1970$ and $y = 10$°N is an average of O_2 at $1968 \leq t < 1972$ and $9.5°N \leq y < 10.5°N$. The error bar indicates ±1 standard error of averaging. The O_2 time series is grouped into three different latitudinal bands: (a) the southern subtropical gyre at 137±0.1°E, (b) the northern part of the 137±0.1°E meridian, off the southern coast of Japan, and (c) the transition area at 144±0.1°E. Lines of different colors correspond to different latitudinal grid points as indicated in legends. (d–f) The same as Figures 5a–5c except that the cases for PO_4 are shown. See supporting information Figures S1–S4 for an extended version of this figure.

anomalies are $r = -0.87$ for the subtropics and $r = -0.71$ for the transition area ($p < 0.01$ for both) (Figure 6). Furthermore, the slope for PO_4 anomalies versus O_2 anomalies is confined to a narrow range of -49 ± 2 for the subtropics and -51 ± 5 for the transition area. The slope for PO_4 anomalies versus O_2 anomalies within the transition area (Figure 6b) differs from the slope for PO_4 trend versus O_2 trend shown in Figure 4b, reflecting strong sensitivity of the estimate to different time spans. More specifically, the difference arises as the declining O_2 trends plateaued since the mid-1990s (Figure 5c), while the increasing PO_4 trends were reversed since the mid-1990s (e.g., 41°N and 42°N in Figure 5f). These deviations after the mid-1990s affect the trend estimates more critically than the anomaly estimates. Nevertheless, the tight association between temporal variations of O_2 and PO_4, which is not explained by the reported stoichiometric ratios of remineralization, is a robust feature, suggesting that biological modulation may not be a primary cause for the O_2 and PO_4 changes on interannual to decadal timescales.

It is noteworthy that compared to moderate changes elsewhere at the 137 ± 0.1°E meridian (Figures 5a and 5d), large interannual fluctuations of O_2 and PO_4 occur within the latitudinal band of 30°–33°N (Figures 5b and 5e). For example, O_2 at 32°N drops sharply by as much as 70 μmol kg^{-1} in the late 1970s, which accompanies a PO_4 increase by 1.2 μmol kg^{-1}. The dramatic changes occurring at 30°–33°N can be attributed to the large meander of the Kuroshio Current south of Japan and the associated cold-core eddy reported for the 1976–1980 time period [*Kawabe*, 1980, 1985; *Sekine and Toba*, 1981; *Nishida*, 1982; *Ishii*, 1982; *Qiu and Joyce*, 1992]. The O_2-rich, PO_4-depleted Kuroshio is deflected equatorward in association with cyclonic eddies that lift the O_2-depleted, PO_4-enriched subsurface water up toward the surface [*Ishii et al.*, 1983; *Tsujino et al.*, 2006].

Taken together, the qualitatively similar structures of O_2 and PO_4 trends (Figures 2 and 3) and the close quantitative association between O_2 and PO_4 variations (Figures 4 and 6) indicate that a large-scale coordinated change has occurred in PO_4 and O_2 distributions between 1968 and 2007. In the next section, we explore trends in oceanic physical properties in the northwest Pacific and a potential cause for the trends.

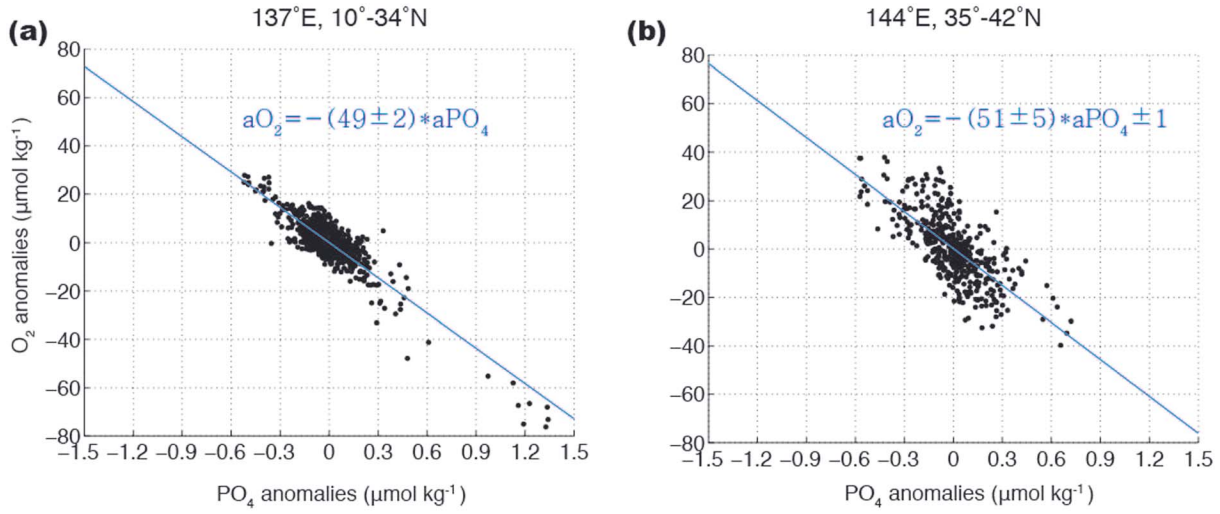

Figure 6. Scatter plots of O_2 anomalies (aO_2) versus PO_4 anomalies (aPO_4), taken from supporting information Figures S1–S4. Anomalies are deviations of the gridded data from the time mean value calculated for each depth and each latitudinal point. (a) The O_2 anomalies (aO_2) versus PO_4 anomalies (aPO_4), taken from Figures S1 and S3 (subtropics). Blue solid line indicates a linear fit to black dots. The ± values represent uncertainties at a 95% significance level. (b) The same as Figure 6a except that the O_2 anomalies (aO_2) versus PO_4 anomalies (aPO_4) taken from Figures S2 and S4 (transition area) are shown.

4. Historical Temperature and Salinity Trends

In order to demonstrate that biogeochemical changes from sparse shipboard observations are consistent with large-scale historical changes in temperature and salinity, we use observationally constrained simulations and estimates. Zonally averaged maps of temperature and salinity trends, computed using SODA2.2.4, are presented in Figures 7b and 7e. The zonally averaged linear trends indicate that between 1950 and 2008 the subsurface water has become cooler and fresher within the transition area at 30°–42°N while the thermocline has become warmer and saltier within the southern subtropical gyre at 10°–20°N (see also Figure 8). The multidecadal trends obtained from the SODA2.2.4 agree with the multidecadal changes obtained by taking the difference of the World Ocean Atlas 2013 (WOA) decadal mean temperature and salinity [*Locarnini et al*., 2013; *Zweng et al*., 2013], which exhibit similar dipole structures (Figures 7a and 7d). Relative to the average over a period of 1955–1974, subsurface waters (150–500 m) have become cooler and fresher north of ~33°N and warmer and saltier south of ~20°N over a period of 1995–2013. Unlike the consistent warming trends at 10°–20°N, which extends up to a 400 m depth, however, salinity increases are mostly confined to shallower depths, shallower than 200 m for the WOA and shallower than 300 m for the SODA2.2.4 within the southern subtropical thermocline. In fact, temporal salinity variations averaged over 140°–180°E, 10°–20°N, 150–400 m display the largest disagreement among the different reanalysis products (Figure 8b), partly due to sparse observations incorporated into the models and analyses.

Nevertheless, both the WOA-based and SODA-based estimates reveal the temperature trend that is roughly opposite between south and north of ~33°N, the latitude across which the meridional gradient of the climatological mean temperature changes its sign (Figure 7). Although this feature is less obvious in the WOA data, SODA salinity also shows that opposite trends have occurred at the northern and southern boundaries of the subtropical gyre. This dipole pattern provides a clue that the multidecadal changes in temperature and salinity over the past decades may be related to meridional movement of the subtropical gyre.

In support of this mechanism, *Joyce and Dunworth-Baker* [2003] attributed multidecadal cooling and freshening of subsurface water within the transition area to a southward shift of the Kuroshio Bifurcation Front, which leads to a southward transport of cold and fresh subpolar water to the transition area [*Nakanowatari et al*., 2015]. Likewise, a southward shift in the southern boundary of the subtropical gyre [*Chen and Wu*, 2012] may replace relatively cold and fresh North Equatorial Current between 10° and 20°N with warmer and saltier subtropical water, thereby explaining increasing temperature and salinity within the southern periphery of the subtropical gyre.

Indeed, we find that significant portions of the subsurface temperature and salinity trends simulated by the SODA2.2.4 (Figures 7b and 7e) can be explained by a southward shift of the subtropical gyre. The best fits to

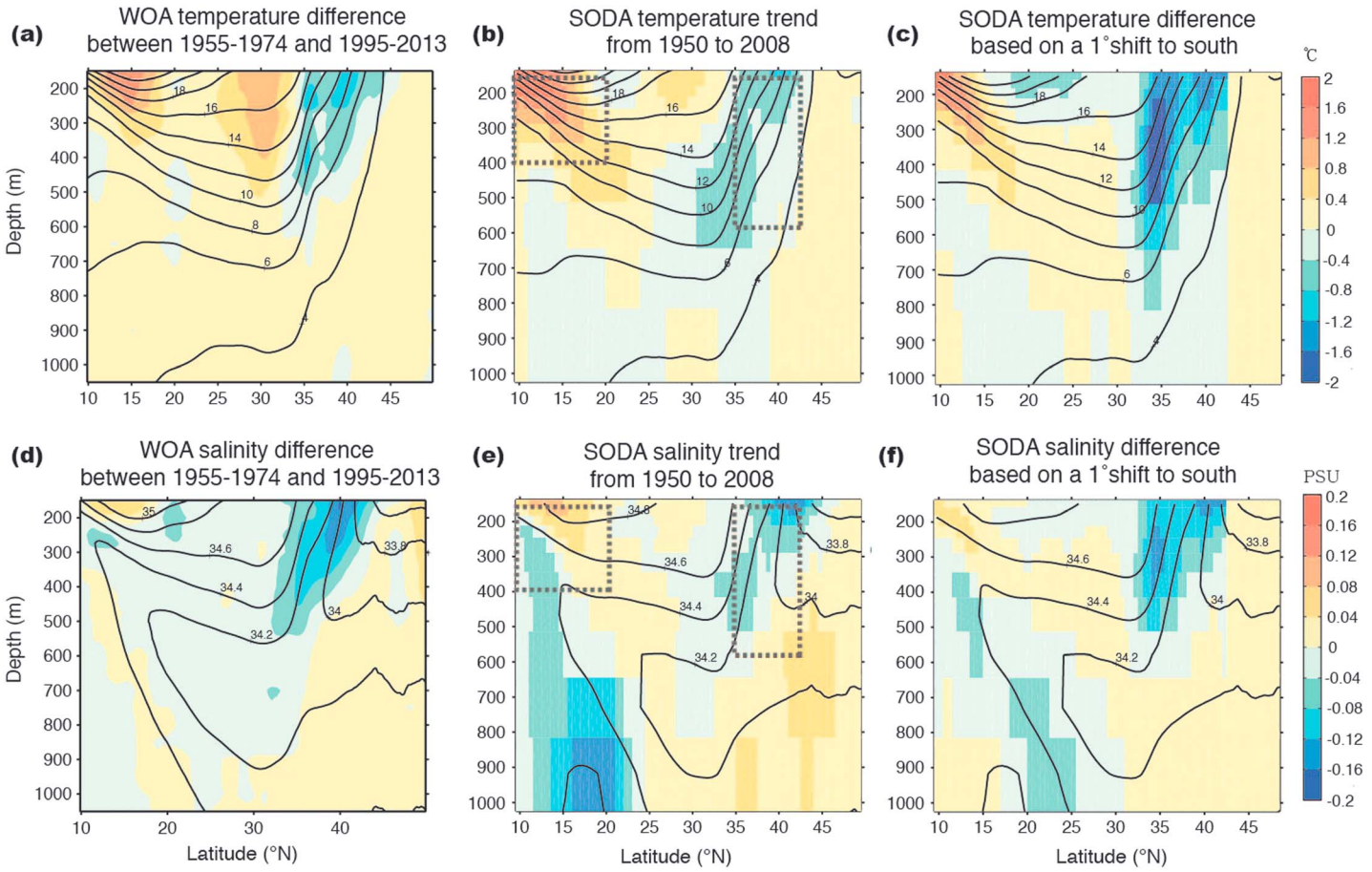

Figure 7. Multidecadal linear trends in temperature and salinity. (a) Color shading indicates zonally averaged (140°–180°E) multidecadal difference of temperature, i.e., the 1995–2003 average minus the 1955–1974 average, computed using the World Ocean Atlas 2013 (WOA). Black solid lines indicate the climatological distribution of temperature averaged between 1955 and 2003. (b) Color shading indicates zonally averaged (140°–180°E) linear trends for temperature from 1950 to 2008, computed using the SODA2.2.4. The unit is in degrees Celsius over the past 50 years. Black solid lines indicate the mean temperature between 1950 and 2008 obtained from the SODA2.2.4. Black dashed boxes indicate the domain over which temperatures are averaged for Figure 8. (c) Zonally averaged temperature changes (color shading) obtained by shifting the climatological mean distribution (solid lines) to the south by 1°, computed using the SODA2.2.4. (d–f) The same as Figures 7a–7c except that the cases for salinity are shown.

the zonally averaged linear trends are obtained from a 1° shift to the south carried out along constant depths ($r = 0.58$ for salinity and $r = 0.78$ for temperature when using the SODA2.2.4) (Figures 7c and 7f). A better agreement between the temporal trends and the 1° shift scenario is obtained when using the SODA2.1.6 ($r = 0.82$ for salinity and $r = 0.86$ for temperature). As shown in Figure 8a, the cooling and freshening tendencies within the transition area are more pronounced in the SODA2.1.6 in a better agreement with the shift patterns (Figures 7c and 7f) than those in the SODA2.2.4.

We suggest that the shift of the subtropical gyre driving multidecadal changes in temperature and salinity in the northwest Pacific is also driving the concomitant changes in PO_4 and O_2 distributions. Indeed, the spatial patterns for O_2 and PO_4 trends over the past 40 years (Figures 3a and 3c) resemble the patterns obtained by shifting their climatological mean distributions to the south by 1° (Figures 3b and 3d). The correlation coefficients between the temporal trends (Figures 3a and 3c) and the expected changes from a 1° shift to the south are $r = 0.62$ for dissolved O_2 and $r = 0.60$ for PO_4. While a southward shift in the northern boundary of the subtropical gyre results in the O_2-depleted and PO_4-enriched subpolar subsurface water being extended to the south, southward shifts in the subtropical recirculation gyre [*Taguchi et al.*, 2007] and the bifurcation latitude of the North Equatorial Current [*Chen and Wu*, 2012] would elevate O_2 and reduce PO_4 in regions where the North Equatorial Current is replaced by relatively well-ventilated, PO_4-depleted subtropical water [*Deutsch et al.*, 2005].

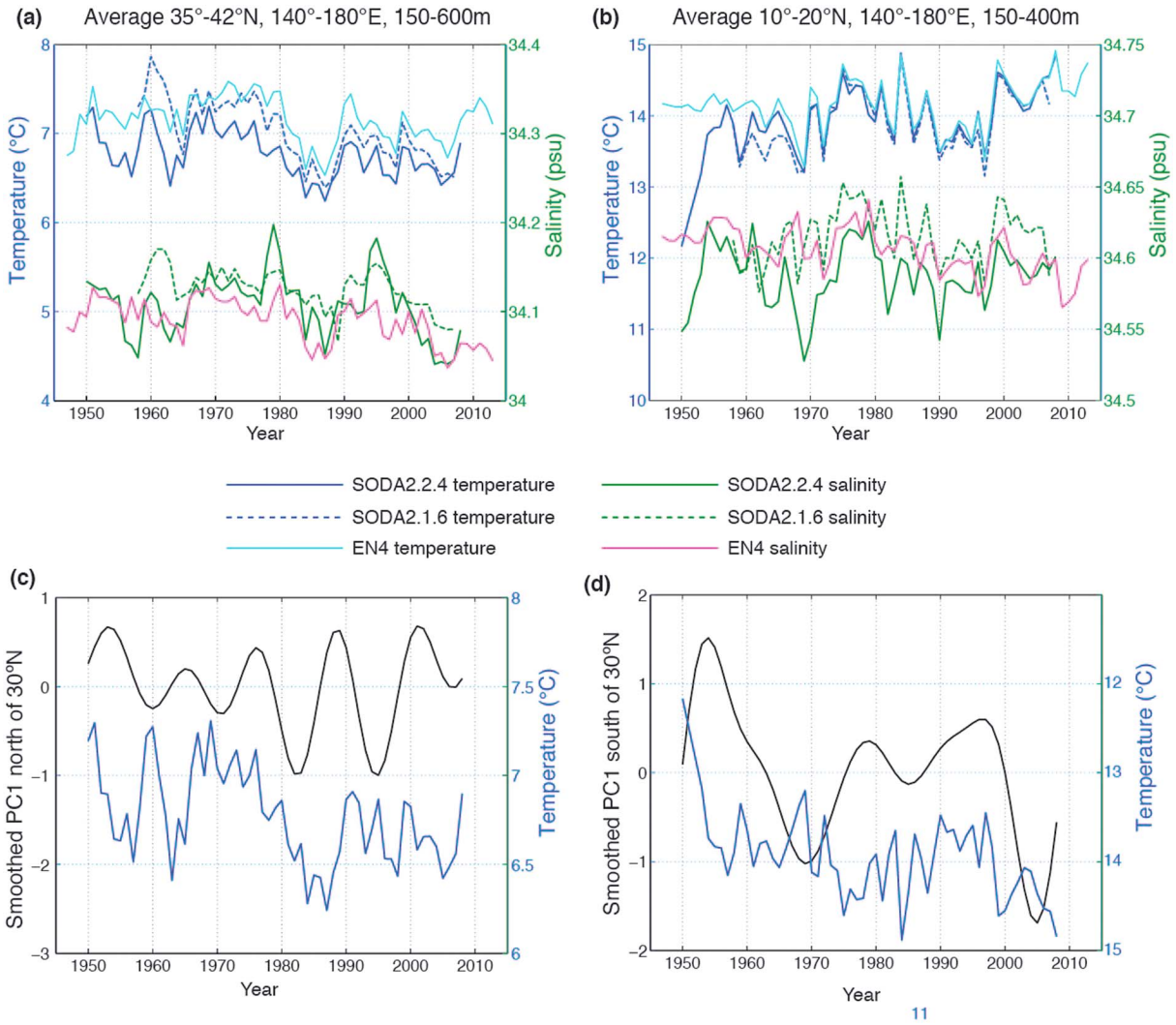

Figure 8. Time series of temperature and salinity averaged within the gyre boundaries, computed using SODA2.2.4, SODA2.1.6, and EN4 data sets. (a) Time series of annual mean temperature (left *Y* axis) and salinity (right *Y* axis) averaged over the northwest Pacific transition area of 35°–42°N, 140°–180°E, 150–600 m. (b) Time series of annual mean temperature (left *Y* axis) and salinity (right *Y* axis) averaged over the southwestern subtropical thermocline of 10°–20°N, 140°–180°E, 150–400 m. Solid blue lines show temperature from SODA2.2.4, dashed blue lines show temperature from SODA2.1.6, and solid cyan lines show temperature from EN4. Solid green lines show salinity from SODA2.2.4, dashed green lines show salinity from SODA2.1.6, and solid magenta lines show salinity from EN4. (c) The SODA2.2.4 temperature change (blue line; shown in Figure 8a) is compared with the low-pass filtered leading PC (PC1) of the Sverdrup stream function, computed for the area north of 30°N (black line; shown in Figure 9b). (d) The SODA2.2.4 temperature change (blue line; shown in Figure 8b) is compared with the low-pass filtered leading PC (PC1) of the Sverdrup stream function, computed for the area south of 30°N (black line; shown in Figure 9d). Note that the right *Y* axis is reversed.

Finally, we note that relative to the large meridional gradients for the climatological mean O_2, PO_4 and temperature (Figures 3b–3d), the meridional gradient for the climatological mean salinity is much weaker within the southern subtropical thermocline (Figure 7f). This means that the same meridional shift in the subtropical gyre would lead to a less pronounced change in salinity within the southern subtropical thermocline. This may partly explain the lack of significant correlations between the southern boundary shift and the salinity change averaged over 140°–180°E, 10°–20°N, 150–400 m (Figures 8b and 8d).

5. The Link Between Winds and Physical/Biogeochemical Tracers

We explore the link between the wind-driven gyre shifts and the variability of temperature, salinity, O_2, and PO_4 within gyre boundaries using observationally constrained simulations and a fully coupled climate model. First, we illustrate how the 20CRv2 wind stress data [*Compo et al.*, 2011] help explain the link between wind-

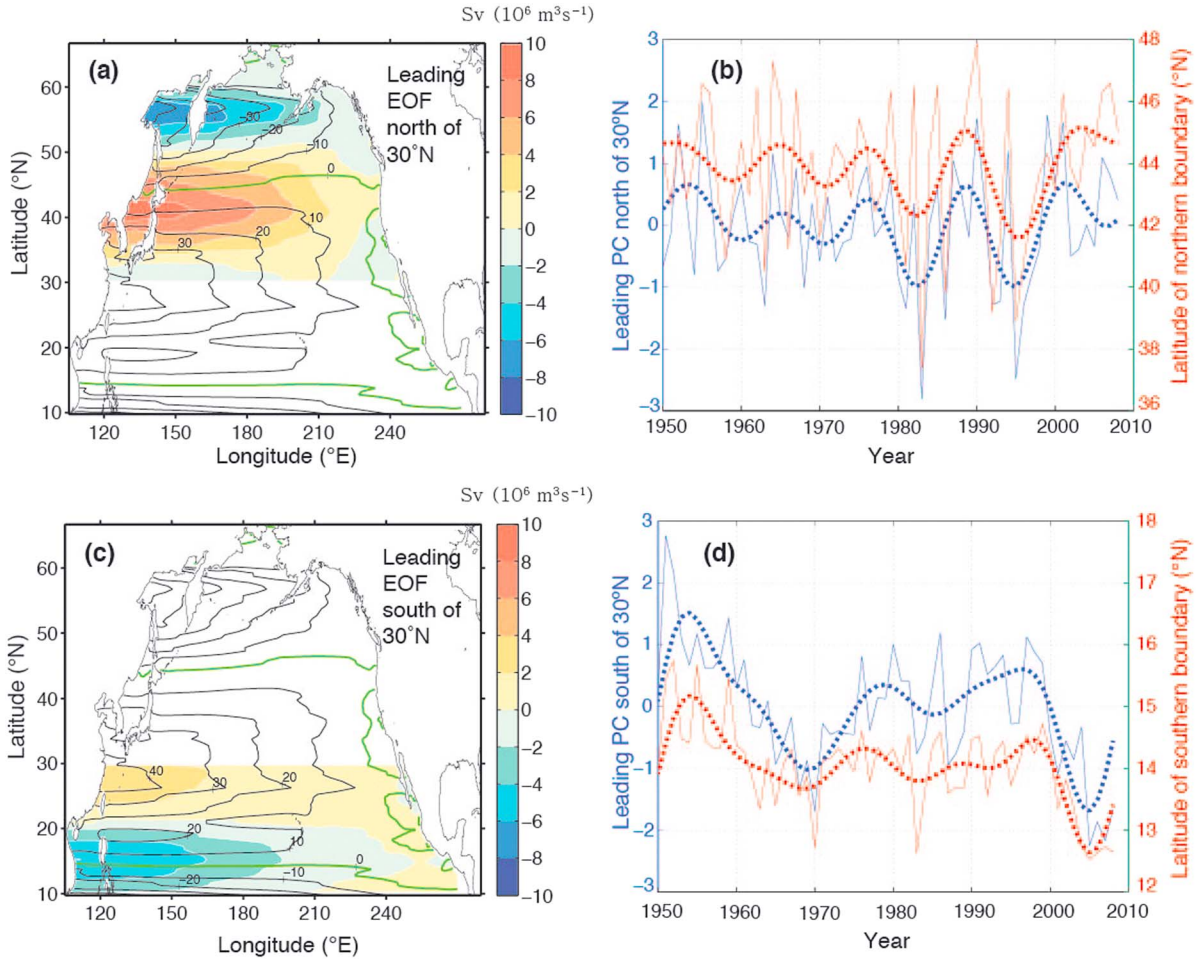

Figure 9. The 20CRv2 diagnostics for gyre boundary shifts. (a) Color shading shows the leading empirical orthogonal function (EOF) of annual mean Sverdrup stream function, computed for the area north of 30°N using the 20CRv2 wind stress from 1950 to 2008. Black contour lines show the climatological mean Sverdrup stream function. Green contour lines show the zero lines of the stream function. (b) Blue thin line shows the associated leading principal component (PC) time series for the area north of 30°N. The low-pass filtered PC is shown in blue dashed line. Red thin line shows the latitude of zero Sverdrup stream function north of 30°N (i.e., the northern boundary). The low-pass filtered latitude variation in the zero stream function is superimposed as red dashed line. (c) The same as Figure 9a except that the leading EOF pattern for the area south of 30°N is shown. (d) The same as Figure 9b except that the leading PC for the area south of 30°N is shown in blue lines. Red lines show the latitude of zero Sverdrup stream function south of 30°N (i.e., the southern boundary).

driven shifts of gyre boundaries and historical variability of temperature and salinity. Then, we demonstrate how the CM2.6 model extends the link to O_2 and PO_4 with a focus on natural biogeochemical variability.

5.1. Historical Gyre Variability From a Reanalysis Data Product

Historical changes in wind-driven gyre circulations are assessed by computing the Sverdrup stream function (section 2.1) using the 20CRv2 annual mean wind stress data [*Compo et al.*, 2011]. The time-averaged distribution of the Sverdrup stream function, which is shown in the solid contour lines of Figures 9a and 9c, indicates a clockwise circulation between 15°N and 45°N and counterclockwise circulations north of ~45°N and south of 15°N. The zero lines of the Sverdrup stream function at ~45°N and ~15°N mark the northern and southern boundaries of the subtropical gyre, respectively.

The empirical orthogonal function (EOF) analysis of the annual mean Sverdrup stream function is performed for three domains of the North Pacific—the entire North Pacific north of 10°N, the area north of 30°N, and the area between 10°N and 30°N—for the period of 1950–2008. The leading EOF modes explain 35%, 45%, and 41% of the total variances of the annual mean Sverdrup stream function for the three domains, respectively. We find that the meridional shifts of the gyre boundaries constitute the dominant modes of the wind-driven gyre variability, with their centers of action all located in the vicinity of the northern and southern gyre

boundaries of the northwest Pacific (Figures 9a and 9c). The leading EOF mode and the associated principal component (PC) time series for the entire North Pacific (not shown) are almost identical to those obtained for the area north of 30°N (Figures 9a and 9b), indicating that the meridional shift of the northern gyre boundary overwhelms the variability elsewhere. When the area south of 30°N is considered, the strong fluctuation along the southern gyre boundary emerges as a dominant mode of the gyre variability within the southern domain (Figure 9c).

The latitudes of the northern and southern boundaries of the subtropical gyre, computed by linearly interpolating the zonally averaged (140°–180°E) Sverdrup stream function into zero, correspond well with the leading PCs (Figures 9b and 9d). The correlation between the latitude of the northern boundary and the leading PC for the area north of 30°N is $r = 0.81$ without applying a low-pass filter and $r = 0.88$ with a filter. The annual mean position of the northern subtropical gyre boundary exhibits large fluctuations on interannual timescales, ranging up to a more than 10° deviation from one year to another. When a low-pass filter is applied to the annual mean values, an overall decreasing trend can be detected at $-0.40 \pm 0.18°$ decade^{-1} between 1950 and 1985. After 1985, trends are nearly absent and decadal-scale fluctuations become dominant instead. The pronounced southward shift in the northern gyre boundary from the 1950s to the 1980s is consistent with the decadal-scale changes in the wind stress curl and the Sverdrup stream function, which occurred in association with the 1976/1977 climate transition [*Deser et al*., 1999].

The multidecadal tendencies of the northern boundary position and the leading PC for the area north of 30°N are roughly in accord with the temperature and salinity variations averaged within the transition area (Figure 8c). For example, the low-pass filtered PC time series correlates moderately with the 4 year lagged annual mean temperatures averaged over 35°–42°N, 140°–180°E, 150–600 m ($r = 0.33$, $p < 0.05$ for SODA2.2.4, $r = 0.32$, $p < 0.05$ for SODA2.1.6, and $r = 0.45$, $p < 0.01$ for EN4, all in which linear trends are removed before calculating correlation coefficients). Southward migration of the northern boundary of the subtropical gyre can cause the subsurface water of the transition area to become cooler and fresher, and vice versa [*Joyce and Dunworth-Baker*, 2003; *Nonaka et al*., 2006]. The multidecadal trend in the northern boundary position of the subtropical gyre also appears to be in accord with PO_4 and O_2 changes observed at the 144°E meridian of the transition area (Figures 5c and 5f) in that PO_4 increases and O_2 decreases are most pronounced until the mid-1990s.

The southern boundary of the subtropical gyre, which is defined here as the latitude of zero Sverdrup stream function south of 30°N, also corresponds well with the leading PC of the Sverdrup stream function computed for the area south of 30°N (Figure 9d). The correlation between the two detrended time series is 0.83 without a low-pass filter and 0.92 with a filter. As in *Chen and Wu* [2012], the southern boundary of the subtropical gyre exhibits an overall southward shift ($-0.18 \pm 0.07°$ decade^{-1}) between 1950 and 2008, with a slight opposing trend between the early 1970s and the late 1990s. For the periods of 1950–1969 and 1993–2008, negative wind stress curl anomalies developed in the latitudinal band of 10°–20°N within the western North Pacific (120°E–150°W), which is favorable to the southward shift of the southern gyre boundary [see *Chen and Wu*, 2012, Figure 4].

The low-pass filtered shifts in the southern boundary of the subtropical gyre and the leading PC for the area south of 30°S are roughly in accord with the annual mean temperature changes averaged over 10°–20°N, 140°–180°E, 150–400 m (Figure 8d). The northward migration of the southern boundary between the early 1970s and the late 1990s coincides with gradual temperature decreases between the mid-1970s and the late 1990s, and the southward migration since the late 1990s coincides with sharp temperature increases since the late 1990s, which is unanimously shown in SODA2.2.4, SODA2.1.6, and EN4 (Figure 8b). Except for the qualitative accordance, however, we do not find any significant correlations between the low-pass filtered variation of the southern boundary position and the detrended temperature changes. The lack of significant correlations within the southern subtropical thermocline may indicate strong modulations of gyre shift effects by ocean circulation changes associated with subtropical mode water formations [*Yamanaka et al*., 2008] and wind wakes due to Hawaiian Islands [*Xie et al*., 2001; *Yamanaka et al*., 2008]. Further studies will be required to fully understand the physical and biogeochemical variability in this complex ocean-atmosphere coupled system.

It is also noteworthy that we do not find any correlations between the positions of the southern and northern boundaries of the subtropical gyre on interannual to decadal timescales. The overall 1° southward shifts in

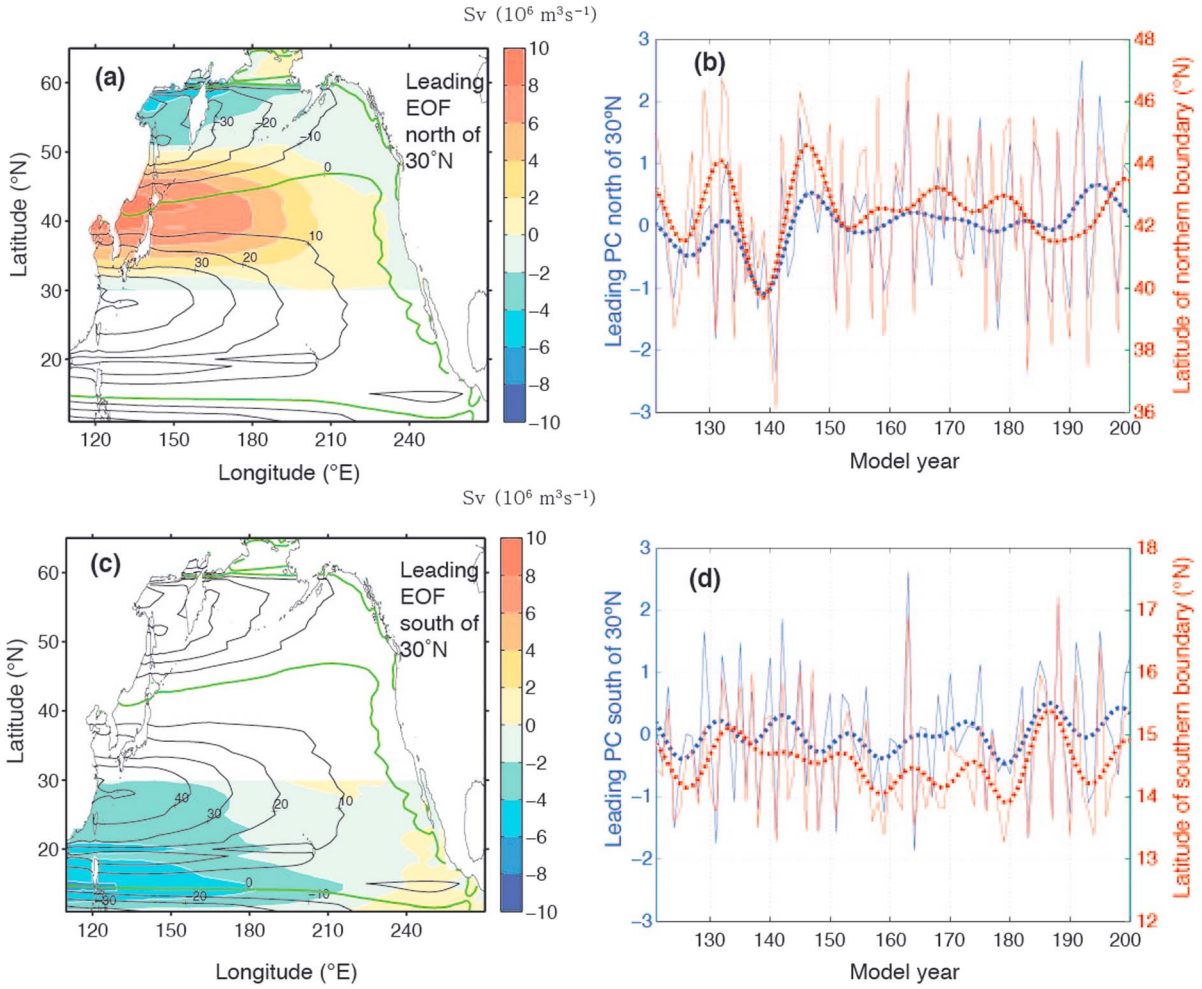

Figure 10. CM2.6 diagnostics for gyre boundary shifts. (a) Color shading shows the leading empirical orthogonal function (EOF) of annual mean Sverdrup stream function, computed for the area north of 30°N using the CM2.6 wind stress from model year 121 to 200. Black contour lines show the climatological mean Sverdrup stream function. Green solid lines show the zero lines of the stream function. (b) Blue thin line shows the associated leading principal component (PC) time series for the area north of 30°N. The low-pass filtered PC is shown in blue dashed line. Red thin line shows the latitude of zero Sverdrup stream function north of 30°N (i.e., the northern boundary). The low-pass filtered latitude variation in the zero stream function is superimposed as red dashed line. (c) The same as Figure 10a except that the leading EOF pattern for the area south of 30°N is shown. (d) The same as Figure 10b except that the leading PC for the area south of 30°N is shown in blue lines. Red lines show the latitude of zero Sverdrup stream function south of 30°N (i.e., the southern boundary).

both boundaries over the past half century might have been simply coincidental. Yet we cannot rule out the possibility that the long-term shifts are due to a long-term response of the ocean to climate change modulated by interanual to decadal ocean-atmosphere feedbacks (see section 6 for a further discussion).

5.2. Consistency With Physical and Biogeochemical Variability in CM2.6

In this section, we use the GFDL CM2.6 to explore multidecadal variations in northwest Pacific temperature, salinity, O_2, and PO_4 and their link to wind-driven shifts in subtropical gyre boundaries. We use the control simulation with preindustrial radiative conditions to shed light on the natural variability. Annual mean values over a spin-up period 121–180 are analyzed, after removing slight model drifts caused by relatively short model integration. The use of the CM2.6 fields complements our analyses of historical observational and reanalysis data sets by providing continuous three-dimensional physical and biogeochemical fields, dynamically consistent and free from observational uncertainties, with a longer time span than available in the observations.

The time mean distribution of the Sverdrup stream function and its dominant modes of the variability obtained from the 20CRv2 (Figure 9) are well captured by the CM2.6 (Figure 10). The leading EOF modes

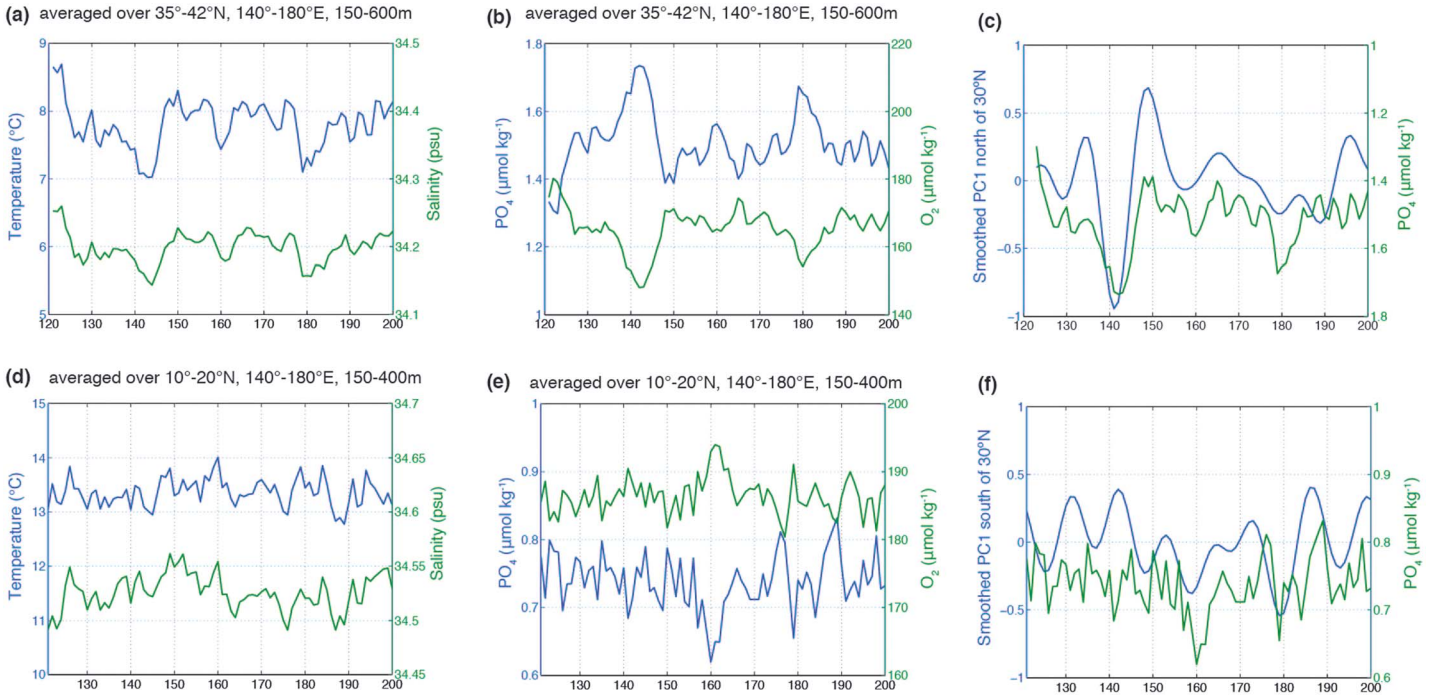

Figure 11. CM2.6 temperature, salinity, PO_4, and O_2 averaged over 35°–42°N, 140°–180°E, 150–600 m. (a) Annual mean temperature (blue) and salinity (green). (b) Annual mean PO_4 (blue) and O_2 (green). (c) The low-pass filtered leading PC (PC1) of the Sverdrup stream function computed for the area north of 30°N (blue line; shown in Figure 10b) is compared with the annual mean PO_4 (green line; shown in Figure 11b). Note that the right *Y* axis for PO_4 concentration is reversed. CM2.6 temperature, salinity, PO_4, and O_2 averaged over 10°–20°N, 140°–180°E, 150–400 m. (d) Annual mean temperature (blue) and salinity (green). (e) Annual mean PO_4 (blue) and O_2 (green). (f) The low-pass filtered latitude variation of the southern boundary (blue line; shown in Figure 10d) and the annual mean PO_4 (green line; shown in Figure 11e).

of the Sverdrup stream function, representing the meridional migration of the gyre boundaries, explain 51% of the total variance for the entire North Pacific north of 10°N, 53% for the area north of 30°N, and 57% for the area south of 30°N. As with the 20CRv2, the leading PCs for the entire North Pacific and the area north of 30°N are correlated well with the meridional migration of the northern gyre boundary, with $r = 0.89$ and $r = 0.87$, respectively, without applying a low-pass filter. With a low-pass filter, the correlation becomes slightly lower at $r = 0.80$ for the entire North Pacific domain and $r = 0.81$ for the area north of 30°N. The leading PC of the Sverdrup stream function for the area south of 30°N also correlates well with the meridional migration of the southern gyre boundary with $r = 0.86$ without a filter and $r = 0.82$ with a filter.

The CM2.6 model shows that the interannual to decadal variations in temperature, salinity, O_2, and PO_4 averaged within the gyre boundaries (over 35°–42°N, 140°–180°E, 150–600 m for the northern boundary and over 10°–20°N, 140°–180°E, 150–400 m for the southern boundary) are all synchronous within the same locations ($|r| > 0.85$ among temperature, salinity, O_2, and PO_4) (Figures 11a, 11b, 11d, and 11e). The high correlations among the tracers highlight ocean physics as a primary factor determining O_2 and PO_4 variations within the gyre boundaries. Reinforcing our findings based on the historical and reanalysis data sets, the physical and biogeochemical properties averaged within the northern boundary of the subtropical gyre faithfully follow the low-frequency variations of the northern boundary position and the leading PC computed for the area north of 30°N (e.g., Figure 11c). Similarly, the physical and biogeochemical properties averaged within the southern boundary of the subtropical gyre correlate well with the low-pass filtered time series of the southern boundary position and the leading PC computed for the area south of 30°N (e.g., Figure 11f).

The maximum correlation coefficients are obtained at a lag of 3 years for the physical and biogeochemical tracers in the northern subtropical gyre boundary ($r = -0.75$ for PO_4, $r = 0.72$ for O_2, $r = 0.70$ for temperature, and $r = 0.67$ for salinity, for all cases significant at 99%). On the other hand, the maximum correlation coefficients are obtained with a lag of 2 years for the tracers within the southern boundary ($r = 0.49$ for PO_4, $r = -0.34$ for O_2, $r = -0.59$ for temperature, and $r = -0.31$ for salinity, for all cases significant at 95%). The correlations become much weaker in the southern subtropical thermocline, partly because high frequency

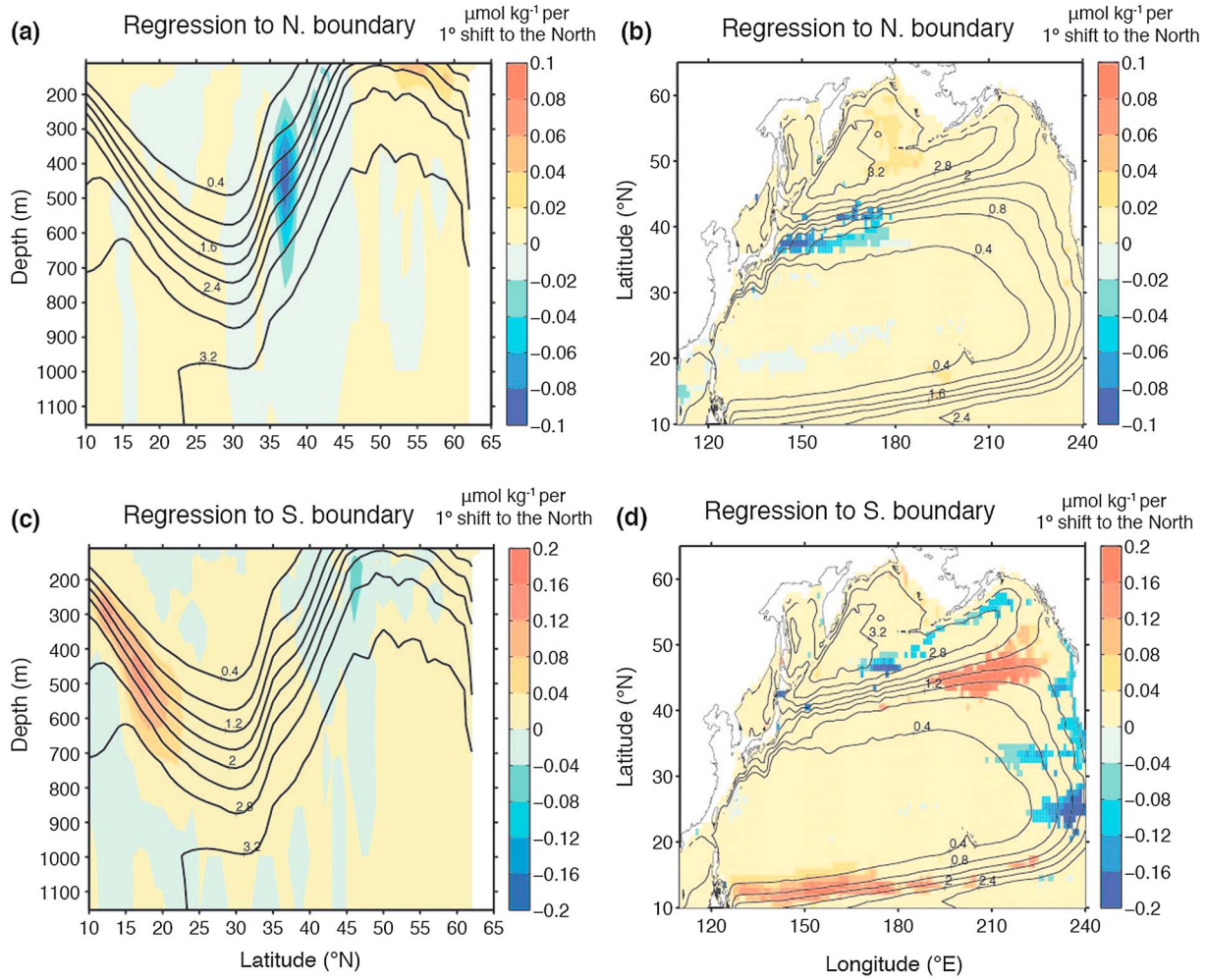

Figure 12. CM2.6 3 year lagged regression of PO_4 on the low-pass filtered latitude change of the gyre boundaries. (a and b) Annual mean PO_4 is regressed on the low-pass filtered variation in the northern boundary (the red dashed line in Figure 10b) with a lag of 3 years. The regression patterns (color shading) are superimposed by the climatological mean PO_4 over model year 121–200 (black contour lines). Figure 12a shows the zonal average between 140°–180°E, and Figure 12b shows a horizontal map at 300 m. (c and d) Annual mean PO_4 is regressed on the low-pass filtered variation in the southern boundary (the red dashed line in Figure 10d) with a lag of 3 years. Values that are not significant at a 95% level are shown as zeros. Northward shifts in the boundaries are positive; thus, the units are in μmol kg^{-1} per a 1° shift to the north. Note that with a southward shift of the gyre by 1° as suggested by observations (see Figure 3), only the polarity changes with the overall regression pattern remaining practically same.

(interannual) fluctuations dominate over low-frequency changes of tracer distributions in low latitudes (Figures 11d and 11e). This point is validated by the fact that the correlation between the low-pass filtered latitudinal change of the southern boundary and the simulated PO_4 improves to $r = 0.68$ (at a 2 year lag) when the low-pass filter is applied to the annual mean PO_4. The lags of up to a few years correspond to the adjustment timescales for the ocean gyres to changes in winds, which is mediated by westward propagating baroclinic Rossby waves responding to wind stress curl forcings [*Deser et al.*, 1999; *Seager et al.*, 2001; *Joyce and Dunworth-Baker*, 2003; *Nonaka et al.*, 2006; *Taguchi et al.*, 2007; *Nakano and Ishikawa*, 2010].

In Figure 12, annual mean PO_4 is regressed onto the low-pass filtered variations in the northern and southern boundary positions (shown as red dashed lines in Figures 10b and 10d) with a 3 year lag. As illustrated in Figure 12, the gyre shift effects are most pronounced within the subsurface (200–700 m) frontal regions of the northern (35°–40°N) and southern (10°–20°N) boundaries of the subtropical gyre. Taken together, this study suggests that North Pacific winds may orchestrate changes in northwest Pacific subsurface O_2 and PO_4, primarily through the north-south movement of gyre boundaries on multidecadal timescales.

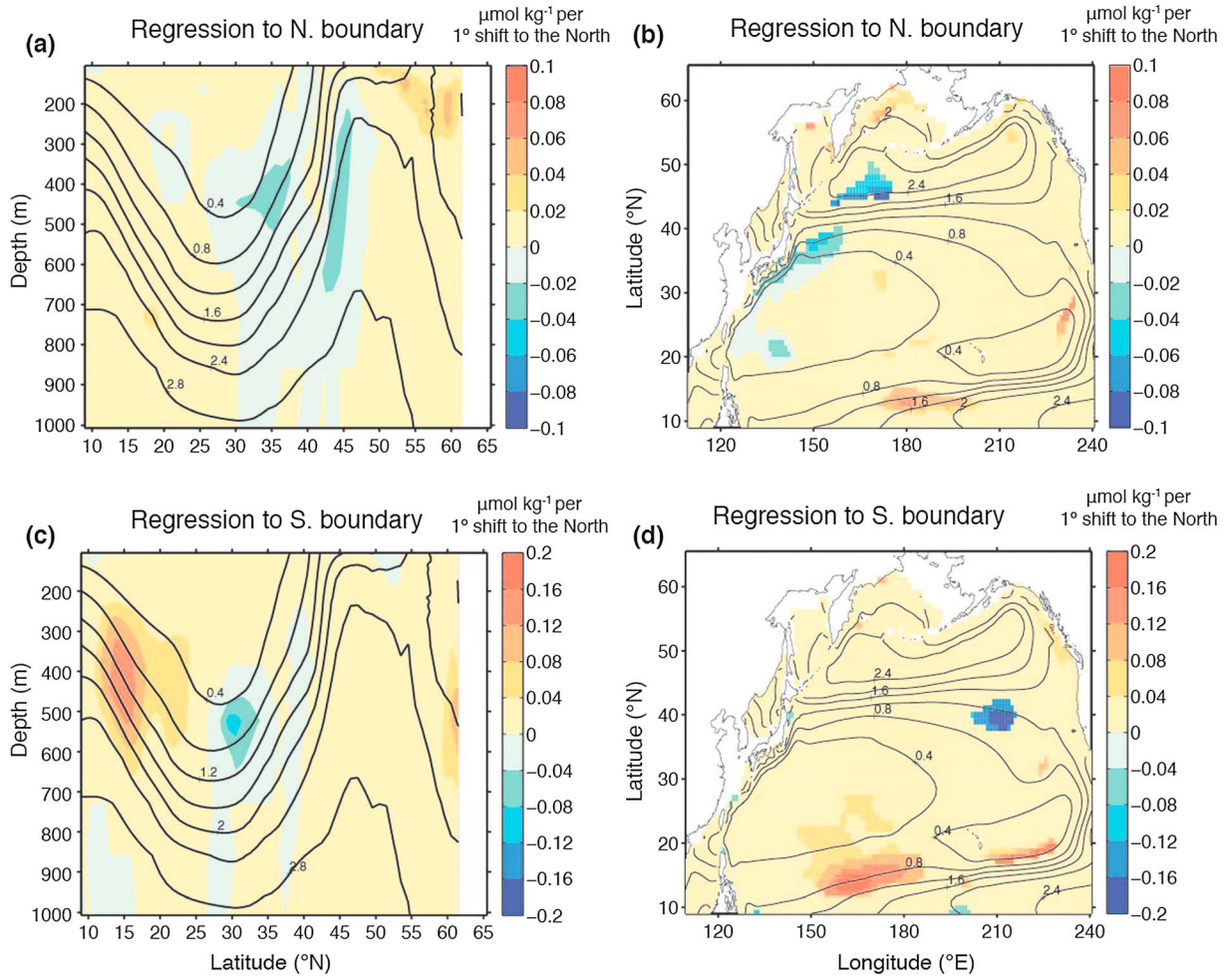

Figure 13. ESM2M 3 year lagged regression of PO_4 on the low-pass filtered latitude change of gyre boundaries. (a and b) Annual mean PO_4 is regressed on the low-pass filtered variation in the northern boundary with a lag of 3 years. The regression patterns (color shading) are superimposed by the climatological mean PO_4 over 1920–1999 (black contour lines). Figure 13a shows the zonal average between 140° and 180°E, and Figure 13b shows a horizontal map at 300 m. (c and d) Annual mean PO_4 is regressed on the low-pass filtered variation in the southern boundary with a lag of 3 years. Values that are not significant at a 95% level are shown as zeros. Northward shifts in the boundaries are positive; thus, the units are in µmol kg^{-1} per a 1° shift to the North.

6. Discussions and Conclusions

Historical data sets reveal contrasting O_2 and PO_4 trends between the subtropical gyre at the 137°E meridian and the transition area at the 144°E meridian in the northwest Pacific (Figures 3a and 3c). Within the transition area, O_2 has decreased by 0.83 ± 0.27 µmol $O_2\,kg^{-1}\,yr^{-1}$ while PO_4 has increased by 0.0054 ± 0.0039 µmol $PO_4\,kg^{-1}\,yr^{-1}$ from 1968 to 2007. Within the subtropical gyre, O_2 has overall increased by 0.29 ± 0.12 µmol $O_2\,kg^{-1}\,yr^{-1}$ and PO_4 has decreased by 0.0050 ± 0.0019 µmol $PO_4\,kg^{-1}\,yr^{-1}$, where the ± ranges denote 95% confidence levels. The spatial patterns of the O_2 and PO_4 trends are similar to the patterns of the SODA temperature and salinity trends, zonally averaged between 140°–180°E, which shows a cooling and freshening trend within the transition area at ~40°N and a warming and salinification trend within the southern subtropical thermocline at ~15°N from 1950 to 2008 (Figures 7b and 7e). Those linear trends are most pronounced within the subsurface water where the meridional gradients of the climatological mean fields are large. These dipole structures led us to posit a southward movement of the northwest Pacific subtropical gyre as a primary cause for the basin-wide coordinated changes in the tracer distributions. These trends in tracer distributions are consistent with overall southward shifts in the subtropical gyre boundaries as suggested by previous studies [*Joyce and Dunworth-Baker*, 2003; *Nonaka et al.*, 2006; *Chen and Wu*, 2012] and also as diagnosed in this study using the Sverdrup stream function.

Despite our results, we note that a significant fraction of the observed trends for O_2 and PO_4 remains unexplained by the southward shift of the subtropical gyre alone (i.e., taking into account only a redistribution of water masses assuming constant ventilation and respiration rates) (see Figure 3). For example, the scenario for a 1° shift to the south tends to underestimate O_2 decline within the transition area by up to 70%. Underestimated O_2 decline near 40°N can reflect the importance of taking into account changes in ocean ventilation rates that may have originated from the Sea of Okhotsk [*Nakanowatari et al*., 2007] and/or from enhanced ocean stratification at the subpolar surface [*Emerson et al*., 2004; *Deutsch et al*., 2005; *Helm et al*., 2011]. In addition, increasing nutrients within the transition area may have increased surface productivity and heterotrophic respiration [*Chai et al*., 2003], which would further decrease O_2 and increase PO_4 in the thermocline. Possible contributions from ocean ventilation changes and biological modulations might have caused the slope for O_2 trend versus PO_4 trend within the transition area to be closer to the reported stoichiometric ratio of remineralization (Figure 4b).

Moreover, wind-driven gyre shifts often accompany changes in the strength of gyre circulations and the properties of subducted mode waters [*Deser et al*., 1996; *Miller et al*., 1998]. The intensification of the southern flank of the Kuroshio Extension Current after the 1976/1977 climate transition [*Deser et al*., 1999] might have led to overall increasing O_2 and decreasing PO_4 at 25°–30°N, which is not explained by the gyre shift effect (Figure 3). Attributing the causes for the changes in the physical and biogeochemical properties along the southern flank of the Kuroshio Extension Current can be challenging as subtropical mode water subduction, current meandering (see a discussion in section 3), mesoscale eddies, and downstream effects of water flows all interact to each other to influence the physical and biogeochemical properties there. The interplay between gyre shifts and ocean circulations/ventilation and its impact on the North Pacific O_2 and PO_4 cycles need to be addressed in future studies.

Although the gyre shift alone does not fully explain observed changes in northwest Pacific physical and biogeochemical properties, our study shows that the role of meridional migration of gyre boundaries is more significant than previously estimated especially within gyre boundaries (10°–20°N and 35°–42°N). The close tie among winds, temperature, salinity, PO_4, and O_2 in the northwest Pacific is clearly demonstrated using the preindustrial simulation of the GFDL CM2.6 model, suggesting that the wind-driven migration explains up to 56% of the physical and biogeochemical properties averaged within the northern gyre boundary and up to 35% for the southern boundary. The important role of gyre shifts in determining the physical and biogeochemical variability within the gyre boundaries is still valid in the climate perturbation simulation where atmospheric CO_2 increases by 1% per year in the CM2.6 model (not shown).

We also note that the large-scale features of the gyre shift effects illustrated using the CM2.6 model (Figure 12) are also captured by the ESM2M [*Dunne et al*., 2012, 2013] in which the ocean model with a nominal resolution of $1° \times 1°$ is coupled with the same ocean biogeochemistry model, miniBLING (Figure 13). However, notable differences can be identified. The ESM2M shows much weaker PO_4 responses to the northern boundary shift, where significant correlations are nearly absent in the eddy-rich transition area between the Kuroshio Current Extension and the Oyashio Front (Figures 13a and 13b). In addition, the meridional gradient of the climatological mean PO_4 is too weak across the southern front of subtropical thermocline in ESM2M, which can be responsible for the lack of significant correlations at 10°–20°N, west of 150°E (Figure 13d). These deficiencies can be attributed partly to poor representations of fronts and mesoscale eddies in the coarse resolution ocean model [*Nonaka et al*., 2006; *Yamanaka et al*., 2008; *Griffies et al*., 2015]. This implies that previous studies using a coarse resolution ocean model may have underestimated the gyre shift effects on tracer variability within gyre boundaries. On the other hand, our results are insensitive to the use of ocean biogeochemistry models of two different complexities: miniBLING [*Galbraith et al*., 2015] and Phytoplankton with Allometric Zooplankton (TOPAZ) [*Dunne et al*., 2013] implemented in ESM2M. This suggests a relatively minor role played by ocean biogeochemical processes in the multidecadal variations in PO_4 and O_2 within the gyre boundaries.

While ocean temperature, stratification, and ventilation changes have been previously recognized as driving variability of the O_2 cycle [e.g., *Keeling and Garcia*, 2002; *Bopp et al*., 2013], we suggest that wind-driven changes in gyre boundaries may play an equally important role for O_2 and PO_4 cycles in the northwest Pacific. Whether the half century southward shifts in North Pacific winds are due to natural variability or to global warming remains highly uncertain. The observed southward shifts are opposite in direction to the

reconstructed/projected northward shifts of subtropical western boundary currents under global warming [*Wu et al*., 2012; *Cheon et al*., 2012]. On the other hand, *Deser et al*. [2015] projected southward shifts in the Northern Hemisphere westerlies and the Intertropical Convergence Zones as a result of competing effects of Arctic sea ice loss and global warming. While further studies are necessary to prove the connection, it is possible that the observed southward shifts in physical and biogeochemical tracers over the past half century might have been a long-term response of the northwest Pacific Ocean to Arctic sea ice loss over the past decades [e.g., *Comiso et al*., 2008]. Our study suggests that subsurface PO_4 and O_2 records within gyre boundaries can be used as an indicator of the meridional movement of gyre boundaries under different climate conditions. Future changes in O_2 and PO_4 within the northwest Pacific will depend not only on changes in temperature, stratification, and ventilation but also on how ocean gyres respond to changes in wind stress forcing, which is the primary driver for trends and variations in the position and intensity of the ocean gyres. One of the keys to the reliable prediction of future marine ecosystems will be the realistic representation of ocean gyre responses to winds and the associated changes in physical and biogeochemical properties.

Acknowledgments

We thank Jorge Sarmiento, Adele Morrison, Seong-Joong Kim, and Min-Ho Kwon for helping improve the manuscript. The World Ocean Database was obtained from https://www.nodc.noaa.gov/OC5/WOD13/. The Simple Ocean Data Assimilation (SODA) outputs along with 20CRv2 wind stress data were obtained from http://www.atmos.umd.edu/~ocean/. The EN4 objectively analyzed monthly mean temperature and salinity data set was obtained from http://www.metoffice.gov.uk/hadobs/en4/. The climatological means as well as the decadal mean fields are obtained from https://www.nodc.noaa.gov/OC5/woa13/woa13data.html. E.Y. Kwon acknowledges NRF-2013R1A1A1058203 award from the National Research Foundation of Korea and "East Asian Seas Time series-I (EAST-I)" award from the Ministry of Oceans and Fisheries, South Korea. Y.H. Kim is supported by the National Research Foundation of Korea (grant NRF-2009-C1AAA001-2009-0093). Y.-G. Park is funded by the project entitled "Development of a satellite based ocean carbon flux model for seas around Korea" from the Ministry of Oceans and Fisheries.

References

Anderson, L. A., and J. L. Sarmiento (1994), Redfield ratios of remineralization determined by nutrient data analysis, *Global Biogeochem. Cycles*, *8*, 65–80, doi:10.1029/93GB03318.

Andreev, A. G., and V. I. Baturina (2006), Impacts of tides and atmospheric forcing variability on dissolved oxygen in the subarctic North Pacific, *J. Geophys. Res.*, *111*, C07S10, doi:10.1029/2005JC003103.

Bopp, L., et al. (2013), Multiple stressors of ocean ecosystems in the 21st century: Projections with CMIP5 models, *Biogeosciences*, *10*, 6225–6245.

Boyer, T. P., et al. (2013), *World Ocean Database 2013*, *NOAA Atlas NESDIS 72*, edited by S. Levitus and A. Mishonov, 209 pp., Silver Spring, Md., doi:10.7289/V5NZ85MT.

Carton, J. A., and B. S. Giese (2008), A reanalysis of ocean climate using Simple Ocean Data Assimilation (SODA), *Mon. Weather Rev.*, *136*, 2999–3017.

Carton, J. A., G. Chepurin, X. Cao, and B. S. Giese (2000a), A simple ocean data assimilation analysis of the global upper ocean 1950–1995, part 1: Methodology, *J. Phys. Oceanogr.*, *30*, 294–309.

Carton, J. A., G. Chepurin, and X. Cao (2000b), A simple ocean data assimilation analysis of the global upper ocean 1950–1995, part 2: Results, *J. Phys. Oceanogr.*, *30*, 311–326.

Chai, F., M. Jiang, R. T. Barber, R. C. Dugdale, and Y. Chao (2003), Interdecadal variation of the transition zone chlorophyll front: A physical-biological model simulation between 1960 and 1990, *J. Oceanogr.*, *59*, 461–475.

Chen, Z., and L. Wu (2012), Long-term change of the Pacific North Equatorial Current bifurcation in SODA, *J. Geophys. Res.*, *117*, C06016, doi:10.1029/2011JC007814.

Cheon, W. G., Y.-G. Park, S.-W. Yeh, and B.-M. Kim (2012), Atmospheric impact on the northwestern Pacific under a global warming scenario, *Geophys. Res. Lett.*, *39*, L16709, doi:10.1029/2012GL052364.

Comiso, J. C., C. L. Parkinson, R. Gersten, and L. Stock (2008), Accelerated decline in the Arctic sea ice cover, *Geophys. Res. Lett.*, *35*, L01703, doi:10.1029/2007GL031972.

Compo, G. P., et al. (2011), The Twentieth Century Reanalysis project, *Q. J. R. Meteorol. Soc.*, *137*, 1–28, doi:10.1002/qj.776.

Delworth, T. L., et al. (2012), Simulated climate and climate change in the GFDL CM2.5 high-resolution coupled climate model, *J. Clim.*, *25*, 2755–2781.

Deser, C., M. A. Alexander, and M. S. Timlin (1996), Upper ocean thermal variations in the North Pacific during 1970–1991, *J. Clim.*, *9*, 1840–1855.

Deser, C., M. A. Alexander, and M. S. Timlin (1999), Evidence for a wind-driven intensification of the Kuroshio extension from the 1970s to the 1980s, *J. Clim.*, *12*, 1697–1706.

Deser, C., R. A. Tomas, and L. Sun (2015), The role of ocean-atmosphere coupling in the zonal-mean atmospheric response to Arctic sea ice loss, *J. Clim.*, *28*, 2168–2186, doi:10.1175/JCLI-D-14-00325.1.

Deutsch, C., S. Emerson, and L. Thompson (2005), Fingerprints of climate change in North Pacific oxygen, *Geophys. Res. Lett.*, *32*, L16604, doi:10.1029/2005GL023190.

DeVries, T., and C. Deutsch (2014), Large-scale variations in the stoichiometry of marine organic matter respiration, *Nat. Geosci.*, *7*, 890–894.

Duchon, C. E. (1979), Lanczos filtering in one and two dimensions, *J. Appl. Meteorol.*, *18*, 1016–1022.

Dufour, C. O., et al. (2015), Role of mesoscale eddies in cross-frontal transport of heat and biogeochemical tracers in the Southern Ocean, *J. Phys. Oceanogr.*, *45*, 3057–3081, doi:10.1175/JPO-D-14-0240.1.

Dunne, J. P., et al. (2012), GFDL's ESM2 global coupled climate–carbon earth system models. Part I: Physical formulation and baseline simulation characteristics, *J. Clim.*, *25*, 6646–6665.

Dunne, J. P., et al. (2013), GFDL's ESM2 global coupled climate–carbon earth system models. Part II: Carbon system formulation and baseline simulation characteristics, *J. Clim.*, *26*, 2247–2267.

Emerson, S., Y. W. Watanabe, T. Ono, and S. Mecking (2004), Temporal trends in apparent oxygen utilization in the upper pycnocline of the North Pacific: 1980–2000, *J. Oceanogr.*, *60*, 139–147.

Fox-Kemper, B., G. Danabasoglu, R. Ferrari, S. M. Griffies, R. W. Hallberg, M. Holland, S. Peacock, and B. Samuels (2011), Parameterization of mixed layer eddies. III: Global implementation and impact on ocean climate simulations, *Ocean Modell.*, *39*, 61–78, doi:10.1016/j.ocemod.2010.09.002.

Galbraith, E. D., A. Gnanadesikan, J. P. Dunne, and M. R. Hiscock (2010), Regional impacts of iron-light colimitation in a global biogeochemical model, *Biogeosciences*, *7*, 1043–1064.

Galbraith, E. D., et al. (2015), Complex functionality with minimal computation: Promise and pitfalls of reduced-tracer ocean biogeochemistry models, *J. Adv. Model. Earth Syst.*, *7*, 2012–2028, doi:10.1002/2015MS000463.

Good, S. A., M. J. Martin, and N. A. Rayner (2013), EN4: Quality controlled ocean temperature and salinity profiles and monthly objective analyses with uncertainty estimates, *J. Geophys. Res. Oceans*, *118*, 6704–6716, doi:10.1002/2013JC009067.

Griffies, S. M. (2012), *Elements of the Modular Ocean Model (MOM): 2012 Release*, *GFDL Ocean Group Tech. Rep. 7*, 618 pp., NOAA/Geophys. Fluid Dyn. Lab., Princeton, N. J.
Griffies, S. M., et al. (2015), Impacts on ocean heat from transient mesoscale eddies in a hierarchy of climate models, *J. Clim.*, *28*, 952–977.
Helm, K. P., N. L. Bindoff, and J. A. Church (2011), Observed decreases in oxygen content of the global ocean, *Geophys. Res. Lett.*, *38*, L23602, doi:10.1029/2011GL049513.
Ishii, H. (1982), Variation of the Kuroshio cold eddy—Large meander of the Kuroshio in 1975–1980 (II), *Rep. Hydrogr. Res.*, *17*, 229–239.
Ishii, H., Y. Sekine, and Y. Toba (1983), Hydrographic structure of the Kuroshio large meander-cold water mass region down to the deeper layers of the ocean, *J. Oceanogr. Soc. Jpn.*, *39*, 240–250.
Joyce, T. M., and J. Dunworth-Baker (2003), Long-term hydrographic variability in the northwest Pacific Ocean, *Geophys. Res. Lett.*, *30*(2), 1043, doi:10.1029/2002GL5225.
Karl, D. M., R. R. Bidigare, and R. M. Letelier (2001), Long-term changes in plankton community structure and productivity in the North Pacific Subtropical Gyre: The domain shift hypothesis, *Deep Sea Res., Part II*, *48*, 1449–1470.
Kawabe, M. (1980), Sea level variations along the south coast of Japan and the large meander in the Kuroshio, *J. Oceanogr. Soc. Jpn.*, *36*, 97–104.
Kawabe, M. (1985), Sea level variations at the Izu Islands and typical stable paths of the Kuroshio, *J. Oceanogr. Soc. Jpn.*, *41*, 307–326.
Keeling, R. F., and H. Garcia (2002), The change in oceanic O_2 inventory associated with recent global warming, *Proc. Natl. Acad. Sci. U.S.A.*, *99*, 7848–7853.
Kwon, E. Y., C. Deutsch, S.-P. Xie, S. Schmidtko, and Y.-K. Cho (2016), The North Pacific oxygen uptake rates over the past half century, *J. Clim.*, *29*, 61–76.
Kwon, Y.-O., M. A. Alexander, N. A. Bond, C. Frankignoul, H. Nakamura, B. Qiu, and L. A. Thompson (2010), Role of Gulf Stream and Kuroshio-Oyashio systems in large-scale atmosphere-ocean interaction: A review, *J. Clim.*, *23*, 3249–3281.
Locarnini, R. A., et al. (2013), *World Ocean Atlas 2013*, *Temperature, NOAA Atlas NESDIS 73*, vol. 1, edited by S. Levitus and A. Mishonov, 40 pp.
Mantua, N. J., S. R. Hare, Y. Zhang, J. M. Wallace, and R. C. Francis (1997), A Pacific interdecadal climate oscillation with impacts on salmon production, *Bull. Am. Meteorol. Soc.*, *78*, 1069–1079.
Miller, A. J., D. R. Cayan, and W. B. White (1998), A westward-intensified decadal change in the North Pacific thermocline and gyre-scale circulation, *J. Clim.*, *11*, 3112–3127.
Nakano, H., and I. Ishikawa (2010), Meridional shift of the Kuroshio Extension induced by response of recirculation gyre to decadal wind variations, *Deep Sea Res., Part II*, *57*, 1111–1126.
Nakanowatari, T., K. I. Ohshima, and M. Wakatsuchi (2007), Warming and oxygen decrease of intermediate water in the northwestern North Pacific, originating from the Sea of Okhotsk, 1955–2004, *Geophys. Res. Lett.*, *34*, L04602, doi:10.1029/2006GL028243.
Nakanowatari, T., H. Mitsudera, T. Motoi, I. Ishikawa, K. I. Oshima, and M. Wakatsuchi (2015), Multidecadal-scale freshening at the salinity minimum in the western part of North Pacific: Importance of wind-driven cross-gyre transport of subarctic water to the subtropical gyre, *J. Phys. Oceanogr.*, *45*, 988–1008.
Nishida, H. (1982), Description of the Kuroshio meander in 1975–1980—Large meander of the Kuroshio in 1975–1980 (I), *Rep. Hydrogr. Res.*, *17*, 181–207.
Nonaka, M., H. Nakamura, Y. Tanimoto, T. Kagimoto, and H. Sasaki (2006), Decadal variability in the Kuroshio-Oyashio Extension simulated in an eddy-resolving OGCM, *J. Clim.*, *19*, 1970–1989.
Ono, T., T. Midorikawa, Y. W. Watanabe, K. Tadokoro, and K. Saino (2001), Temporal increases of phosphate and apparent oxygen utilization in the subsurface waters of western subarctic Pacific from 1968 to 1998, *Geophys. Res. Lett.*, *28*, 3285–3288, doi:10.1029/2001GL012948.
Palter, J. B., M. S. Lozier, and R. T. Barber (2005), The effect of advection on the nutrient reservoir in the North Atlantic, *Nature*, *437*, 687–692.
Qiu, B., and T. M. Joyce (1992), Interannual variability in the mid- and low-latitude western North Pacific, *J. Phys. Oceanogr.*, *22*, 1062–1079.
Redfield, A. C. (1934), On the proportions of organic derivations in sea water and their relation to the composition of plankton, in *James Johnstone Memorial Volume*, edited by R. J. Daniel, pp. 176–192 , Univ. Press of Liverpool, Cambridge, U. K.
Sasano, D., Y. Takatani, N. Kosugi, T. Nakano, T. Midorikawa, and M. Ishii (2015), Multidecadal trends of oxygen and their controlling factors in the western North Pacific, *Global Biogeochem. Cycles*, *29*, 935–956, doi:10.1002/2014GB005065.
Seager, R., Y. Kushnir, N. H. Naik, M. A. Cane, and J. Miller (2001), Wind-driven shifts in the latitude of the Kuroshio-Oyashio extension and generation of SST anomalies on decadal timescales, *J. Clim.*, *14*, 4149–4165.
Sekine, Y., and Y. Toba (1981), Velocity variation of the Kuroshio during the small meander formation south of Kyushu, *J. Oceanogr. Soc. Jpn.*, *37*, 87–93.
Smith, R. D., J. K. Dukowicz, and R. C. Malone (1992), Parallel ocean general circulation modeling, *Physica D*, *60*, 38–61, doi:10.1016/0167-2789(92)90225-C.
Stramma, L., A. Oschlies, and S. Schmidtko (2012), Mismatch between observed and modeled trends in dissolved upper-ocean oxygen over the last 50 yr, *Biogeosciences*, *9*, 4045–4057.
Sverdrup, H. U. (1947), Wind-driven currents in a baroclinic ocean; with application to the equatorial currents of the eastern Pacific, *Proc. Natl. Acad. Sci. U.S.A.*, *33*, 318–326, doi:10.1073/pnas.33.11.318.
Tadokoro, K., T. Ono, I. Yasuda, S. Osafune, A. Shiomoto, and H. Sugisaki (2009), Possible mechanisms of decadal-scale variation in PO_4 concentration in the western North Pacific, *Geophys. Res. Lett.*, *36*, L08606, doi:10.1029/2009GL037327.
Taguchi, B., S.-P. Xie, N. Schneider, M. Nonaka, H. Sasaki, and Y. Sasai (2007), Decadal variability of the Kuroshio Extension: Observations and an eddy-resolving model hindcast, *J. Clim.*, *20*, 2357–2377.
Takatani, Y., D. Sasano, T. Nakano, T. Midorikawa, and M. Ishii (2012), Decrease of dissolved oxygen after the mid-1980s in the western North Pacific subtropical gyre along the 137°E repeat section, *Global Biogeochem. Cycles*, *26*, GB2013, doi:10.1029/2011GB004227.
Tsujino, H., N. Usui, and H. Nakano (2006), Dynamics of Kuroshio path variations in a high-resolution general circulation model, *J. Geophys. Res.*, *111*, C11001, doi:10.1029/2005JC003118.
Watanabe, Y. W., M. Wakita, N. Maeda, T. Ono, and T. Gamo (2003), Synchronous bidecadal periodic changes of oxygen, phosphate and temperature between the Japan Sea deep water and the North Pacific intermediate water, *Geophys. Res. Lett.*, *30*(24), 2273, doi:10.1029/2003GL018338.
Whitney, F. A., H. J. Freeland, and M. Robert (2007), Persistently declining oxygen levels in the interior waters of the eastern subarctic Pacific, *Prog. Oceanogr.*, *75*, 179–199.
Whitney, F. A., S. J. Bograd, and T. Ono (2013), Nutrient enrichment of the subarctic Pacific Ocean pycnocline, *Geophys. Res. Lett.*, *40*, 2200–2205, doi:10.1002/grl.50439.
Wu, L., et al. (2012), Enhanced warming over the global subtropical western boundary currents, *Nat. Clim. Change*, doi:10.1038/NCLIMATE1353.

Xie, S.-P., W. T. Liu, Q. Liu, and M. Nonaka (2001), Far-reaching effects of the Hawaiian Islands on the Pacific Ocean-atmosphere system, *Science*, *292*, 2057–2060.

Yamanaka, G., H. Ishizaki, M. Hirabara, and I. Ishikawa (2008), Decadal variability of the Subtropical Front of the western North Pacific in an eddy-resolving ocean general circulation model, *J. Geophys. Res.*, *113*, C12027, doi:10.1029/2008JC005002.

Zweng, M. M., et al. (2013), *World Ocean Atlas 2013*, *Salinity, NOAA Atlas NESDIS 74*, vol. 2, edited by S. Levitus and A. Mishonov, 39 pp.